



Analysis of impulsive ground motions from February 2023 Kahramanmaraş earthquake sequence

Deniz Ertuncay^{1,2} · Giovanni Costa¹

Received: 2 August 2023 / Accepted: 8 March 2024
© The Author(s) 2024

Abstract

On the 6th of February 2023, a large magnitude earthquake (Pazarcık earthquake), $M_w = 7.7$, occurred in southeast Türkiye, which caused significant destruction in Türkiye and Syria. Relatively large magnitude aftershocks followed the main shock, and after 9 hours of the main event, another large magnitude earthquake (Elbistan earthquake) occurred, $M_w = 7.6$, on a nearby fault. This study analyzes the near-fault seismic signals from earthquakes larger than 5.5 recorded between the main shock and the 31st of March 2023. More than 60 impulsive motions are detected in 3 earthquakes, mostly concentrated in the Pazarcık and Elbistan earthquakes. In the Pazarcık earthquake, many impulsive motions are recorded in near-fault stations with periods of up to 14 s. In contrast, in the Elbistan earthquake, impulsive motions are spatially distributed, with pulse periods of up to 11 s and at distances greater than 150 km. Pulse periods mostly correlate with the magnitude of the earthquake, but pulse probability models do not predict impulsive motions over long distances. The presence of strong impulsive motions in vertical components is also observed. For both earthquakes, peak ground velocities (PGVs) are larger than predicted by ground motion prediction equations. The observation of long-period, large amplitude signals may indicate the presence of a directivity effect for both earthquakes. In some stations, spectral periods exceed the 2018 Turkish building design codes for long periods (≥ 1 s).

Keywords Kahramanmaraş earthquakes · Impulsive ground motion · Near-fault ground motion · Strong motion

✉ Deniz Ertuncay
dertuncay@ogs.it

Giovanni Costa
costa@units.it

¹ Department of Mathematics and Geoscience, SeisRaM Working Group, University of Trieste, Via E. Weiss, 4, Trieste 34127, Italy

² Center for Seismological Research, National Institute of Oceanography and Applied Geophysics - OGS, Via Treviso, 55, Udine 33100, Italy

1 Introduction

On the 6th of February 2023 at 01:17:32 UTC a $M_w = 7.7$ earthquake hit southeast Türkiye and Syria. The earthquake initiated on the small Nurdağı-Pazarcık Fault (NPF) but then jumped to the East Anatolian Fault (EAF, Survey USG 2023a; Melgar et al. 2023; Okuwaki et al. 2023). Only 9 h after the $M_w = 7.7$ earthquake the region was hit by another major earthquake with $M_w = 7.6$ that occurred on the Sürgü Fault (SF, Survey USG 2023b; Melgar et al. 2023; Okuwaki et al. 2023). The result of the two major earthquakes in such a short interval was devastating for the region, with a death toll of around 59000 people (≈ 51000 in Türkiye and ≈ 8000 in Syria). The region is well known for its high seismic hazard (Akkar et al. 2018) and risk (Crowley et al. 2021) with numerous active faults and historic seismicity (Erdik 2013) and large population (Gunasekera et al. 2023). In fact, the 6th of February earthquakes occurred in a region where the largest ground motions are expected in Türkiye (Fig. 1).

Thanks to the dense strong motion station coverage in the near-fault region, a large amount of seismic data was collected during the Kahramanmaraş earthquakes. Near-fault ground motion provides valuable information related to earthquake physics (e.g. directivity effects) and ground deformation (e.g. the fling step effect). If the earthquake rupture propagates towards seismic stations, forward directivity can be observed in stations where the cumulative effect of the rupture arrives in a short window of time with a long period and large amplitude (Somerville et al. 1995). Permanent ground deformation can also be seen in seismic signals (Bolt 2002) and can be identified as impulsive

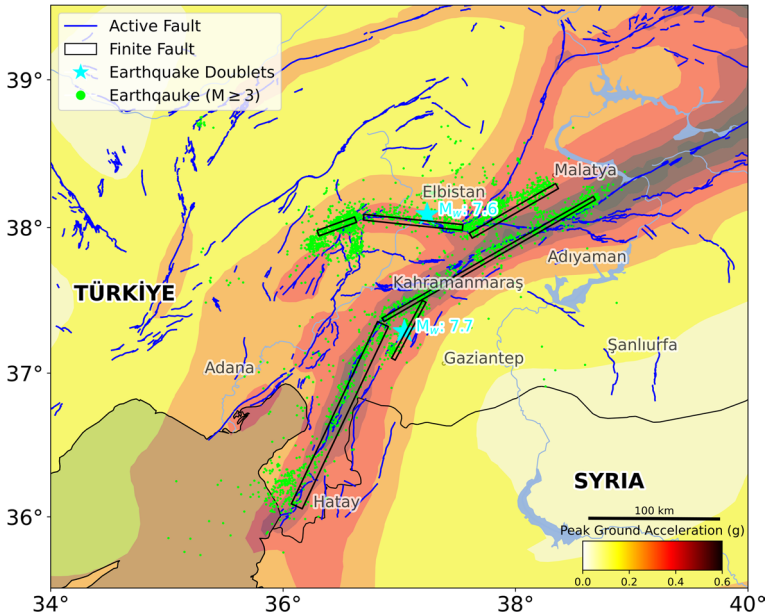


Fig. 1 Earthquakes ($M \geq 3.0$, green dots) and seismic hazard map (Danciu et al. 2021) of south-east Türkiye and Syria. Seismic hazard is for 10 % probability of exceedance in 50 years for soil condition (V_{s30}) = 760 ms^{-1} . Blue lines show the active fault lines (Emre et al. 2018), cyan stars show the epicentres of the Kahramanmaraş doublet earthquakes, and the black rectangles identify finite fault solutions from (Survey USG 2023a, b)

signals. Moreover, site amplification may further amplify impulsive signals (Kobayashi et al. 2019).

Impulsive signals may magnify the destructive effects of earthquakes by creating large seismic demands on structures and infrastructure such as: masonry buildings (Shabani et al. 2023), (i) seismically isolated structures (Bhagat et al. 2021), (ii) reinforced concrete structures (Carocci 2012), (iii) industrial buildings (Zhang et al. 2021), (iv) minarets (Oliveira et al. 2012), (v) bridges (Li et al. 2017; Chen et al. 2022), (vi) wind turbines (Ali et al. 2020), (vii) dams (Gorai and Maity 2021), and (viii) warehouses (Hatayama 2008). Velocity pulses, in general, have high energy at the beginning of the shaking, which may lead to large deformation and damage with respect to non-impulsive signals. Since the impulsive motion concentrates the seismic energy in one or few pulses with a specific period, it may create large inelastic demand on structures with fundamental periods close to the period of the impulsive motion (Kalkan and Kunnath 2006).

In this study, we analyze strong motion records (see Sect. 2) from the Kahramanmaraş earthquakes to detect and analyze the impulsive ground motions. We used the methods of Shahi and Baker (2014), Ertuncay and Costa (2019) as detection algorithms. Shahi and Baker (2014) use the NGA-West 2 database (Ancheta et al. 2014) to define what impulsive motion is and provides the detection algorithm that is explained below. Ertuncay and Costa (2019) use NGA-West 2, GeoNet (GNS Science 2020), the Italian Accelerometric Archive (Pacor et al. 2011), and K-Net databases (Earth Science and Resilience 2019). We also analyze the probability of observing impulsive motion with the models of Shahi and Baker (2014), Ertuncay and Costa (2021), described in Sect. 3. We present individual impulsive motions in Sect. 4 and discuss their features in Sect. 5.

2 Data

After the first shock of the Kahramanmaraş sequence, there are more than 3057 earthquakes ($M \geq 3.0$) registered by Disaster and Emergency Management Authority (AFAD; deprem.afad.gov.tr/event-catalog, last access: 14/06/2023) between 6th of February 2023 and 31st of March 2023. In total, 287879 traces are collected from the Turkish National Seismic Network (52 stations) (Disaster and Emergency Management Authority 1990), the Turkish National Strong Motion Network (143 stations) (Disaster and Emergency Management Authority 1973), and Kandilli Observatory and Earthquake Research Institute (KOERI, 6 stations) (Kandilli Observatory And Earthquake Research Institute 1971; Cambaz et al. 2021), all of which are recorded from accelerometric stations. The location of the earthquakes and stations is presented in Fig. 2 and EC8 site classification of the stations is given in Table 1. In this study, we analyze the traces of 15 earthquakes with a magnitude larger than 5.5 (Table 2).

For the analysis, continuous data from AFAD database (tdvms.afad.gov.tr/continuous_data, last access: 14/06/2023) are downloaded and the traces are cut starting from 5 s before the theoretical P-wave arrival (calculated using the velocity structure of (Kennett and Engdahl 1991)) until 90 s after the theoretical P-wave arrival. We then perform the following processing on the raw data: (i) removal of the instrument response (ii) detrending (ii) 4th order Butterworth band-pass filtering between 0.02 Hz to 10 Hz (iv) Cumulatively integrate (cumtrapz integration) acceleration waveforms to velocity waveforms using the composite trapezoidal rule, (v) detrending (vi) visual inspection to pick and remove signals with visible anomalies (e.g. large data gaps)

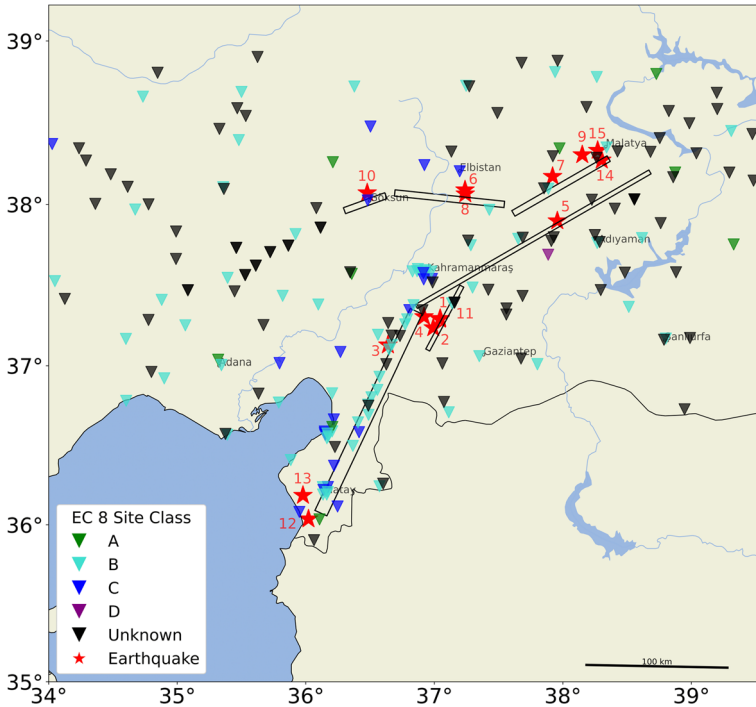


Fig. 2 Earthquakes and seismic stations used in this study along with their site classes according to Eurocode 8 (EC8, Aucun et al. 2012). Black boxes are the finite fault solutions for the Pazarçık and Elbistan earthquakes as performed by USGS (Survey USG 2023a, b)

Table 1 EC8 site classes of the stations used in this study

EC8 class	Number of stations
A	11
B	69
C	22
D	1
Unknown	98

3 Method

In this study, we use the algorithms of Shahi and Baker (2014) and Ertuncay and Costa (2019) to detect impulsive motions in Kahramanmaraş earthquakes. Pulse detection algorithms are explained in Sect. 3.1. Moreover, the probability of observing impulsive motion is calculated for the events that created at least one impulsive motion are analyzed by using the models developed by Shahi and Baker (2014) and Ertuncay and Costa (2021). The models are explained in Sect. 3.2. Finally, periods of the impulsive motions are compared with magnitude-pulse period relations that are introduced in Sect. 3.3.

Table 2 Events from Kahramanmaraş sequence used in this study

Event ID	Date (UTC)	Longitude	Latitude	Magnitude	Location
1	2023-02-06 01:17:32	37.043	37.288	7.7	Pazarcık (Kahramanmaraş)
2	2023-02-06 01:26:49	36.992	37.235	5.6	Nurdağı (Gaziantep)
3	2023-02-06 01:28:16	36.92	37.304	6.6	Nurdağı (Gaziantep)
4	2023-02-06 01:36:28	36.639	37.128	5.7	Hasanbeyli (Osmaniye)
5	2023-02-06 02:03:35	37.957	37.898	5.6	Doğanşehir (Malatya)
6	2023-02-06 10:24:47	37.239	38.089	7.6	Elbistan (Kahramanmaraş)
7	2023-02-06 10:26:46	38.271	38.332	5.8	Yeşilyurt (Malatya)
8	2023-02-06 10:32:08	37.241	38.064	5.5	Ekinözü (Kahramanmaraş)
9	2023-02-06 10:35:57	37.92	38.172	5.9	Doğanşehir (Malatya)
10	2023-02-06 10:51:30	38.151	38.305	5.7	Yeşilyurt (Malatya)
11	2023-02-06 12:02:11	36.478	38.071	5.9	Göksun (Kahramanmaraş)
12	2023-02-06 20:37:51	37.046	37.293	5.5	Pazarcık (Kahramanmaraş)
13	2023-02-20 17:04:27	36.021	36.037	6.4	Yayladağı (Hatay)
14	2023-02-20 17:07:34	35.978	36.186	5.8	Samandağ (Hatay)
15	2023-02-27 09:04:49	38.303	38.272	5.6	Yeşilyurt (Malatya)

3.1 Detection of impulsive signals

To detect impulsive motions methods of Shahi and Baker (2014) and Ertuncay and Costa (2019) are selected. The methods are neither modified nor updated by using the data collected for this study. Shahi and Baker (2014) use wavelet analysis to detect the impulsive motion and the pulse period (T_p) of a given velocity time history using a 4th order Daubechies wavelet. They analyse the frequency characteristics of the signal using the continuous wavelet transform (CWT). CWT coefficients are combined linearly to rotate the signal in arbitrary directions. Depending on the direction, the signal with the most energetic features is determined. PGV, which is also orientation-dependent, is also retrieved. To analyze the signals in a similar manner as Ertuncay and Costa (2019), instead of two orthogonal components a single component is given as an input. However, as given in Sect. 4, orthogonal component analyses are also carried out to find the direction of impulsive motions as a separate analysis. By using the CWT coefficients, the concentration of the seismic energy is defined over a relatively small time and frequency window, one of the indicators of impulsive motion. A wavelet is created by using the largest coefficient, and the fitted Daubechies wavelet is subtracted from the original waveform to calculate the PGV ratio between the original signal and the residual signal. Principal component (PC) analysis between the PGV ratio and the ratio between the squared original signal and the squared residual signal (*energy ratio*) are performed, and the following relation is developed:

$$PC = 0.63 \times (PGV \text{ ratio}) + 0.777 \times (\text{energy ratio}). \tag{1}$$

Support vector classification is introduced by analyzing the PC, and PGV of the signals and pulse indicator (PI) boundary is defined as below:

$$PI = 9.384 \times (0.76 - PC - 0.0616PGV) \times (PC + 6.914 \times 10^{-4}PGV - 1.072) - 6.179. \tag{2}$$

A given signal is identified as impulsive if PI gets a positive value. For instance, Station 4611 (Fig. 3) has a maximum PGV of 81.24 cm/section (it is larger than the original PGV of the waveform due to the arbitrary rotation part of the process), PI of 1.28, and PC of 0.85.

Ertuncay and Costa (2019) also use wavelet analysis to detect impulsive motion. The wavelet transformation of a given velocity domain signal is carried out using both Ricker and Morlet wavelets. The concentration of the seismic energy is found in the wavelet domain by computing the wavelet power spectrum (WPS) of the signal, and depending on the location of the maximum energy, two different approaches are used.

If the maximum energy is located where the PGV is observed in the time history of the signal, the algorithm checks if PGV is larger than 30 cms^{-1} . If it is larger than the threshold, then the period of maximum WPS is considered as T_p , and it is used for further steps. The starting (t_s) and ending (t_e) points of the impulsive part of the waveform are determined using the time instance of PGV as the centre of the impulsive part, and cover the area between t_s and t_e (the PGV area). If the mean of WPS energy and the squared velocity time history of the pulse area is larger than 30 % of the entire waveform, then the signal is considered as impulsive.

The alternative pulse location is also considered by Ertuncay and Costa (2019) by allowing the maximum WPS to be different to the PGV position. In this case, the maximum amplitude where WPS is located should be larger than 25 cms^{-1} , and both the WPS and the squared velocity time history of the pulse area must contain at least 10 % more energy than the PGV area. Furthermore, the mean of the WPS energy and the squared velocity time history of the alternative pulse area must be larger than 30 % of the entire waveform. In Fig. 3 the impulsive part of the earthquake carries 67.35 % of the waveform energy and 60.77 % of the WPS energy.

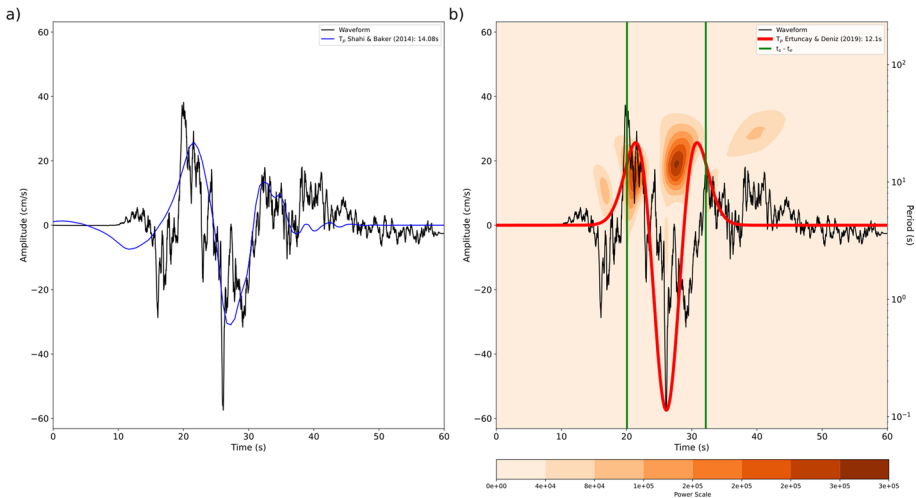


Fig. 3 Velocity time history record of the Pazarcık earthquake in the fault-normal component of Station 4611 with impulsive motion extracted using the methods of **a**Shahi and Baker (2014), and **b** Ertuncay and Costa (2019)

3.2 Probability of impulsive motion

Shahi and Baker (2014) developed two models to determine the probability of observing impulsive signals for a given earthquake. These models are developed both for impulsive motion due to the directivity effect and for regular impulsive motion. To develop the models, a linear combination of several parameters related to strike-slip and non-strike-slip faults has been used. These parameters are: (i) the length of the fault from the epicentre to the point in which the distance between a site of interest and the fault is minimum (s), (ii) the closest distance from the site of interest to the ruptured fault (R) and (iii) the angle between the lines of the fault plane and the line between the epicentre and the site of interest (θ).

The models are as in below:

$$\begin{aligned}
 P(\text{directivity}|R, s, \theta, \text{strike} - \text{slip}) &= \frac{1}{1 + e^{0.7897+0.1378R-0.3533\sqrt{s}+0.020\theta}} \\
 P(\text{pulse}|R, s, \theta, \text{strike} - \text{slip}) &= \frac{1}{1 + e^{0.4570+0.1260R-0.2440\sqrt{s}+0.013\theta}}
 \end{aligned}
 \tag{3}$$

Ertuncay and Costa (2021) also develop two models for strike-slip and non-strike-slip faults using a multivariate naïve Bayes classifier. They use parameters: (i) M_w , (ii) Joyner-Boore distance (the shortest distance from a site to the surface projection of the rupture plane), (R_{jb}), and (iii) source-to-site azimuth (Kaklamanos et al. 2011).

The strike-slip model dataset in Ertuncay and Costa (2021) contains earthquakes with magnitudes between 5.7 to 7.9, which covers the magnitude of earthquakes analysed in this paper.

3.3 Pulse period comparison

Periods of the impulsive motions that are determined by the methods explained in Sect. 3.1 are compared with the pulse period estimation algorithms. There are various approaches to detect the longest period. These approaches include the earthquake magnitude (Somerville 2003; Bray and Rodriguez-Marek 2004; Shahi and Baker 2014; Ertuncay 2020) and parameters related to the earthquake kinematics (e.g. rise time, rupture speed); earthquake and station relations (e.g. the distance between the ruptured fault and a site of interest); and the velocity structure of the earthquake area (Fayjaloun et al. 2017; Scala et al. 2018). In this study, we focus only on the algorithms that provide a relation between M_w and T_p , since studies related to these parameters are not in agreement in terms of earthquake kinematics, and these parameters are the most likely to vary during rupture (Melgar et al. 2023; Barbot et al. 2023). A comparison between the calculated pulse periods and predictions from previously developed equations is presented in Table 3.

Table 3 Relations between M_w and T_p used in this study

Relation	Standard deviation (σ)	Design case	Reference
$\log(T_p) = 0.5 M_w - 3.17$	0.80	Rock sites	
$\log(T_p) = 0.35 M_w - 2.02$	0.62	Soil sites	Somerville (2003)
$\ln(T_p) = 1.32 M_w - 8.60$	0.40	Rock sites	
$\ln(T_p) = 0.93 M_w - 5.60$	0.58	Soil sites	Bray and Rodriguez-Marek (2004)
$\ln(T_p) = 1.08 M_w - 6.26$	0.61	Directivity related pulses	
$\ln(T_p) = 1.12 M_w - 6.55$	0.57	General pulses	Shahi and Baker (2014)
$\ln(T_p) = 0.85 M_w - 4.65$	0.51	General pulses	Ertuncay (2020)

4 Results

In total we detect 72 impulsive signals using the Shahi and Baker (2014) algorithm and 62 impulsive signals using the Ertuncay and Costa (2019) algorithm. Those signals are observed in 3 earthquakes, the Pazarcık (Kahramanmaraş), Nurdağı (Gaziantep), and Elbistan (Kahramanmaraş) events.

4.1 Pazarcık earthquake ($M_w = 7.7$)

The Pazarcık earthquake (Event ID: 1) initiated in the relatively small NPF (Segment 1), which intersects with EAF). EAF, then, bilaterally ruptured in two different segments. The first segment ruptured towards the North-East (Segment 2), and the second segment ruptured towards the South-West (Segment 3, Survey USG 2023a; Melgar et al. 2023; Okuwaki et al. 2023). A large number of impulsive signals have been detected from this earthquake thanks to the dense station coverage along Segment 3 (Fig. 4). Even though most of the impulsive motions are recorded in the very near-fault stations, pulse-shaped signals are recorded at distances of up to $R_{jb} \simeq 78$ km from the fault (Fig. 5). The first impulsive motion detected in Station 4615 has the closest epicentral distance, R_{epi} , and most of the seismic energy arrives at the station in a single pulse. Due to the multi-segment nature of the earthquake, some of the stations have $R_{jb} = 0$ km despite having $R_{epi} \simeq 150$ km (e.g. Station 3124). As a result of the complex rupture, some stations, such as Station 4620 and Station 3115, show impulsive motion whilst having waveforms that are energetic for almost 60 s, which is unusual as impulsive motion tends to result in rather simple seismic traces (Somerville 2003).

To detect impulsive motions, stations are rotated from East–West and North–South orthogonal components to fault-normal and fault-parallel components using the strike angles of each segment, which are 28° , 60° , and 25° for Segments 1–3, respectively. The strike angle of the closest segment to each station is used for the rotation. The same method is applied for the Elbistan earthquake. In total we find 40 impulsive signals using the Shahi and Baker (2014) method and 55 impulsive signals using the Ertuncay and Costa (2019) method. Among the impulsive motions, 17 and 25 of them are in the fault-parallel direction, 14 and 18 of them are in the fault-normal direction, and 9 and 12 of them are in the vertical component for Shahi and Baker (2014) and Ertuncay and Costa (2019) methods, respectively (Table 4). The maximum pulse period of the impulsive motion is up to 15.6 s

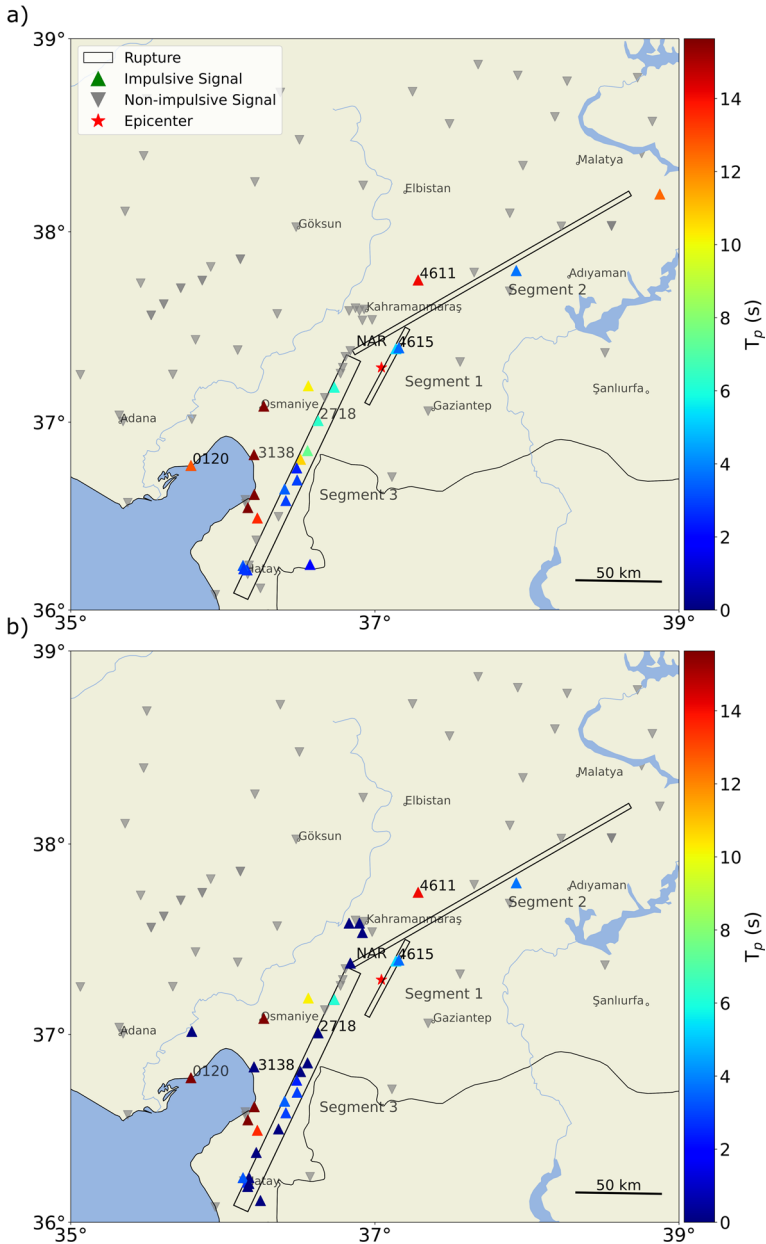


Fig. 4 Impulsive signals detected by **a**Shahi and Baker (2014) **b** Ertuncay and Costa (2019) from the Pazarçık earthquake. The red star is the epicentre of the event retrieved from the AFAD catalogue, and the black boxes are the ruptured segments as defined by USGS (2023a)

in Station 0120 (Fig. 6). In the velocity response spectra of this station, there are two distinctive peaks around ≈ 7 s and ≥ 10 s and the Shahi and Baker (2014) method effectively detects the latter one as impulsive, as in the response spectra of the residual waveform the

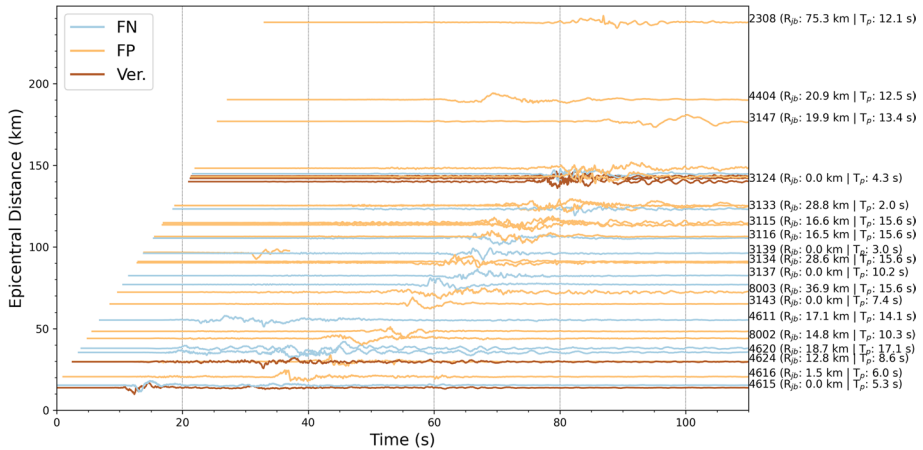


Fig. 5 Velocity time histories of impulsive signals recorded from the Pazarcık earthquake. In the case of impulsive motion in more than one orientation for a given station, the velocity time history of the channel with the largest T_p is selected. FN, FP, and Ver. represent fault-normal, fault-parallel, and vertical components, respectively

second peak vanishes and the spectral amplitudes of the wavelet fitted by Shahi and Baker (2014) and the recorded signal match.

To calculate the probabilities of occurrence of impulsive motions we use the Shahi and Baker (2014), Ertuncay and Costa (2021) methods. The Shahi and Baker (2014) method works only for a single fault rupture. To use the model for multiple segments, we move the epicentre position to the edges of the segments that are closer to the epicentre for Segments 2 and 3 (personal communication with J. W. Baker). Finite source models of Pazarcık (Survey USG 2023a) and Elbistan (Survey USG 2023b) earthquakes show that the dip angle of the ruptured faults are not 90° , hence the surface projection of the faults cover an area instead of a line. To calculate the probabilities of observing impulsive motions with the model of Shahi and Baker (2014) as given in Eq. 3, upper edge of the ruptured fault is considered as the rupture line.

Most of the impulsive signals are detected in areas with a large probability of observing impulsive motion, as determined by both models (Fig. 7). However, several non-impulsive signals in the near-fault region are close to the impulsive stations. For instance, there are 7 stations without impulsive motions in the area where Segment 2 and Segment 3 meet. Some of these stations, however, did not record the entire earthquake due to data transmission problems. Station 0213, on the other hand, recorded an impulsive motion even though it only recorded the first 20 s of the event. In this regard, non-impulsive stations in this area can be ignored for the evaluation of the pulse occurrence models. Outliers such as Stations 0120 ($R_{jb} = 65.16$ km), 2308 ($R_{jb} = 75.25$ km), and 0125 ($R_{jb} = 78.40$ km) are located in the low probability zones for impulsive motion.

4.2 Nurdağı earthquake ($M_w = 6.6$)

Nurdağı earthquake (Event ID: 3) is the largest aftershock of the Kahramanmaraş earthquakes with $M_w = 6.6$. It occurred 11 minutes after the main shock and in between the second and third segments of the Pazarcık earthquake. Most of the impulsive signals

Table 4 Parameters of impulsive signals in Pazarcik earthquake

Station	Component	STLA	STLO	Vs30 (cm s ⁻¹)	R _{jb} (km)	PGA (cm s ⁻²)	PGV (cm s ⁻¹)	T _p Ertuncay and Costa (2019) [s]	T _p Shahi and Baker (2014) [s]
0120	FP	36.77	35.79	296*	65.16	132.35	31.11	14.39	15.64
	FN					115.97	25.63	0.0	12.8
0125	FP	37.02	35.8	228*	78.4	122.96	33.26	12.1	0.0
	FP	37.8	37.93	752*	4.52	227.13	100.43	3.6	8.9
0213	FN					207.32	58.59	3.6	4.19
	Ver					300.89	32.14	3.6	3.74
2308	FP	38.45	39.31	450	75.25	376.96	39.5	12.1	0.0
2712	FP	37.18	36.73	495*	0.0	739.11	111.87	7.19	0.0
	FN					510.31	84.9	6.05	6.15
2718	FP	37.01	36.63	415*	0.0	641.21	121.88	6.05	6.3
	Ver					586.69	52.54	5.09	0.0
3115	FP	36.55	36.16	424	16.65	211.55	57.13	12.1	15.62
3116	FP	36.62	36.21	870	16.55	182.37	31.16	7.19	7.98
	FN					179.21	46.79	12.1	15.64
3123	FN	36.21	36.16	470	0.0	602.1	171.6	2.14	2.67
3124	Ver	36.24	36.17	283	0.0	578.68	42.27	4.28	0.0
	Ver	36.24	36.13	448	2.37	1233.09	67.45	3.02	3.32
3126	Ver	36.22	36.14	350	0.9	1085.14	71.25	0.0	2.76
	FP	36.19	36.16	567	0.0	340.45	45.2	7.19	0.0
3131	FN					379.94	50.29	10.17	0.0
	FP	36.21	36.17	377	0.0	494.42	72.22	14.39	0.0
3133	FN	36.24	36.57	377	28.78	208.02	43.33	0.0	2.0
	FP	36.83	36.2	374	28.61	250.79	50.7	12.1	15.55
3134	FN					227.76	35.69	5.09	0.0

Table 4 (continued)

Station	Component	STLA	STLO	Vs30 (cm s ⁻¹)	R _{jb} (km)	PGA (cm s ⁻²)	PGV (cm s ⁻¹)	T _p Ertuncayy and Costa (2019) [s]	T _p Shahi and Baker (2014) [s]
3136	FP	36.12	36.25	344	4.64	396.31	52.5	10.17	0.0
	Ver					223.57	31.31	4.28	0.0
3137	FP	36.69	36.49	688	0.0	647.82	85.37	8.55	9.55
	FN					703.51	86.36	10.17	10.19
	Ver					485.83	44.39	3.6	2.95
3138**	FP	36.8	36.51	618	0.0	799.88	236.95	5.09	0.0
	FN					770.27	166.47	7.19	10.7
	Ver					1408.91	107.06	28.77	0.0
3139	FP	36.58	36.41	272	0.0	600.24	161.38	2.64	0.0
	FN					531.72	140.89	2.54	2.98
3141	FP	36.37	36.22	338	1.58	687.19	92.96	4.45	0.0
3142	FP	36.5	36.37	539	0.0	798.44	79.68	12.1	0.0
3143	FP	36.85	36.56	444	0.0	340.79	130.52	7.19	7.42
	FN					382.47	59.76	6.05	0.0
3144	FP	36.76	36.49	485	0.0	458.46	93.52	7.19	8.4
	FN					826.1	120.28	10.17	8.93
	Ver					445.91	79.07	2.54	2.45
3145	FP	36.65	36.41	533	0.0	807.28	140.74	8.55	8.81
	FN					525.88	110.23	4.28	4.73
	Ver					619.64	64.19	3.02	3.44
3146	FP	36.49	36.23	767*	7.54	386.29	50.73	12.1	13.55
3147	FP	35.9	36.06	519*	19.94	47.83	26.66	0.0	13.38
4404	FP	38.2	38.87	1380	20.85	122.36	28.07	0.0	12.5

Table 4 (continued)

Station	Component	STLA	STLO	Vs30 (cm s ⁻¹)	R _{jb} (km)	PGA (cm s ⁻²)	PGV (cm s ⁻¹)	T _p Ertuncay and Costa (2019) [s]	T _p Shahi and Baker (2014) [s]
4611	FP	37.75	37.28	731	17.14	314.71	35.73	6.05	6.68
	FN					377.32	57.39	12.1	14.08
4615	FP	37.39	37.14	484	0.0	486.73	136.79	3.6	4.44
	FN					619.27	104.7	5.09	4.35
4616	Ver					675.05	69.94	5.09	5.28
	FP	37.38	36.84	390	1.48	697.47	86.9	6.05	0.0
4617	FN					552.1	60.39	3.02	0.0
	FP	37.59	36.83	574	21.81	151.8	33.53	17.11	0.0
4620	FN	37.59	36.9	484	18.67	303.6	42.66	17.11	0.0
	Ver	37.54	36.92	280	12.77	164.06	35.91	8.55	0.0
8002	FP	37.19	36.56	430	14.84	205.77	55.8	8.55	10.26
	FN	37.08	36.27	350	36.86	190.43	41.82	14.39	15.64
KHIMN	FP	37.39	37.16	248*	0.0	518.1	88.23	4.28	4.47
	Ver					418.74	39.14	3.6	4.16
NAR	FN	37.39	37.16	248*	0.0	577.12	102.35	3.6	4.48
	Ver					485.13	45.22	3.6	3.65

Vs30s with * are predicted by the (Oktay 2022) method due to a lack of information on the AFAD website. FP, FN, and Ver. represent fault-parallel, fault-normal, and vertical components. ** Issues with the vertical component of Station 3138 are discussed in Sect. 5

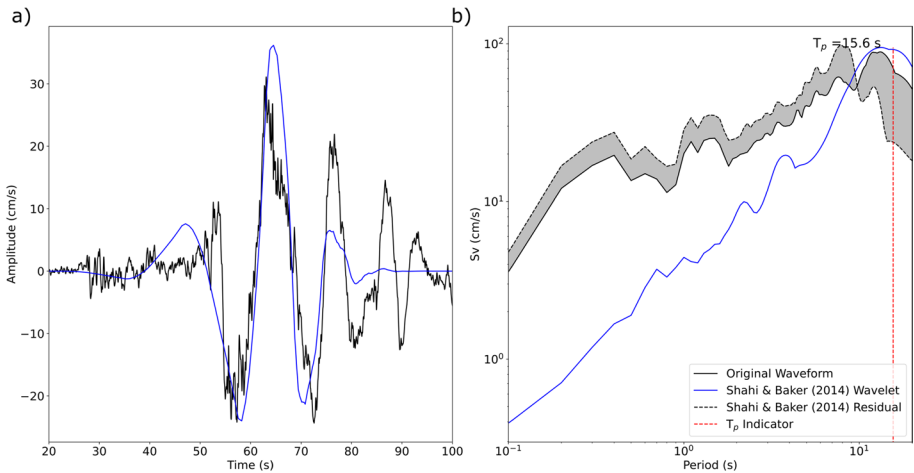


Fig. 6 **a** Velocity time history of Station 0120 in Pazarçık earthquake (black) and the wavelet fitted by the Shahi and Baker (2014) method, and **b** velocity response spectra of the station, the wavelet, and residuals between the velocity waveform and the wavelet. Grey area defines the contribution of the impulsive part of the signal on the velocity response spectra

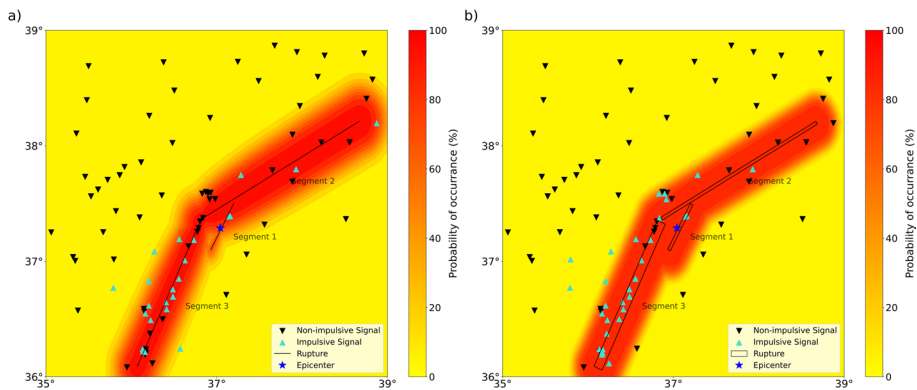


Fig. 7 Probability of observing impulsive motion from **a**Shahi and Baker (2014) and **b** Ertuncay and Costa (2021) methods for the Pazarçık earthquake. The blue star is the epicenter of the event, and black and turquoise triangles are the non-impulsive and impulsive stations, respectively

are located near the epicentre with R_{epi} less than 50 km (Fig. 8). Velocity time histories of the impulsive motions are simpler than the Pazarçık earthquake, and most of their seismic energy is concentrated at the beginning of the waveform as epicentral distances are short. Unlike the Pazarçık and Elbistan earthquakes, no finite fault model has been developed for this earthquake yet. Hence R_{jb} , and fault-normal & fault-parallel information are not retrieved for the earthquake. They can be developed using relations such as Wells and Coppersmith (1994), but the complex ruptures of the Pazarçık and Elbistan earthquakes show that the rupture area of the Nurdağı could have a complex structure too. The point source approach has been implemented to prevent incorrect interpretation of the impulsive motion of the earthquake.

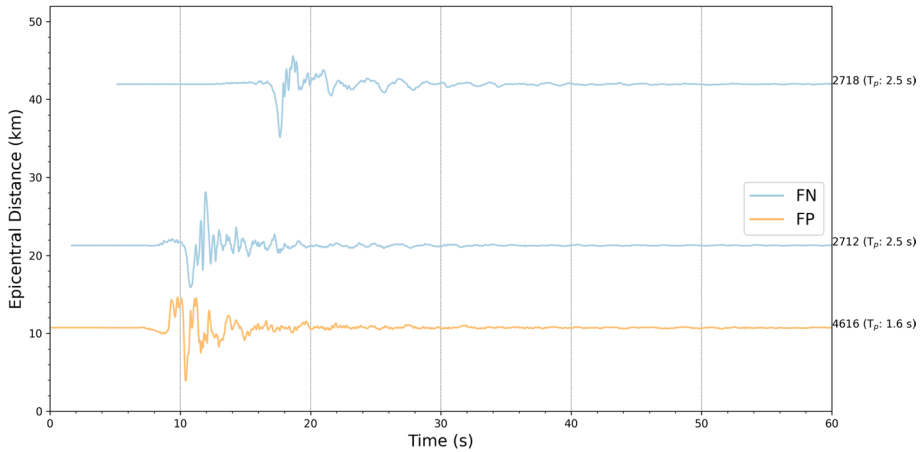


Fig. 8 Velocity time histories of impulsive signals recorded in Nurdağı earthquake

To detect impulsive motions, stations are rotated from East–West and North–South orthogonal components to fault-normal and fault-parallel using the strike angle of the event with the assumption that the Nurdağı earthquake ruptured a single segment. The focal plane solution of AFAD (<https://deprem.afad.gov.tr/event-detail/408329>, last access: 30/11/2023) estimates the strike angles as 300° and 187° . Between these, we believe that 300° is the strike angle of the fault plane since it is in agreement with the seismicity of the Kahramanmaraş sequence, whereas 187° is the strike angle of the auxiliary plane. In total Shahi and Baker (2014) and Ertuncay and Costa (2019) found 5 and 2 impulsive signals, respectively (Fig. 9). Among the impulsive motions, (Shahi and Baker 2014) detected 2 impulsive motions in the fault-parallel and another 2 impulsive motions in the fault-normal components, whereas (Ertuncay and Costa 2019) detected only 2 impulsive motions in the fault-normal component. Moreover, a vertical component impulsive motion is also detected by Shahi and Baker (2014) (Table 5). Pulse periods of the impulsive motions in the earthquake are rather short, up to 2.5 s (Fig. 10). The Ertuncay and Costa (2019) method fits a Ricker wavelet to the impulsive motion and, by nature of the wavelet, there are two valleys on each side of the central lobe that fit into the PGV on the time domain. However, in the recorded signal, there is no such motion, which creates unexpectedly large spectral periods in the fitted wavelet. Apart from the larger spectral periods of the fitted wavelet, the pulse period is captured as spectral periods of the residual signal have no features in periods around 2.1 s.

4.3 Elbistan earthquake ($M_w = 7.6$)

Elbistan earthquake (Event ID: 6) is the second destructive earthquake of the Kahramanmaraş earthquakes, which happened only nine hours after the Pazarcık earthquake. The earthquake was initiated on the SF fault, and the rupture was bilateral with 3 ruptured segments (Survey USG 2023b; Melgar et al. 2023; Okuwaki et al. 2023). The earthquake initiated in the first segment and ruptured bilaterally to the west and northeast segments.

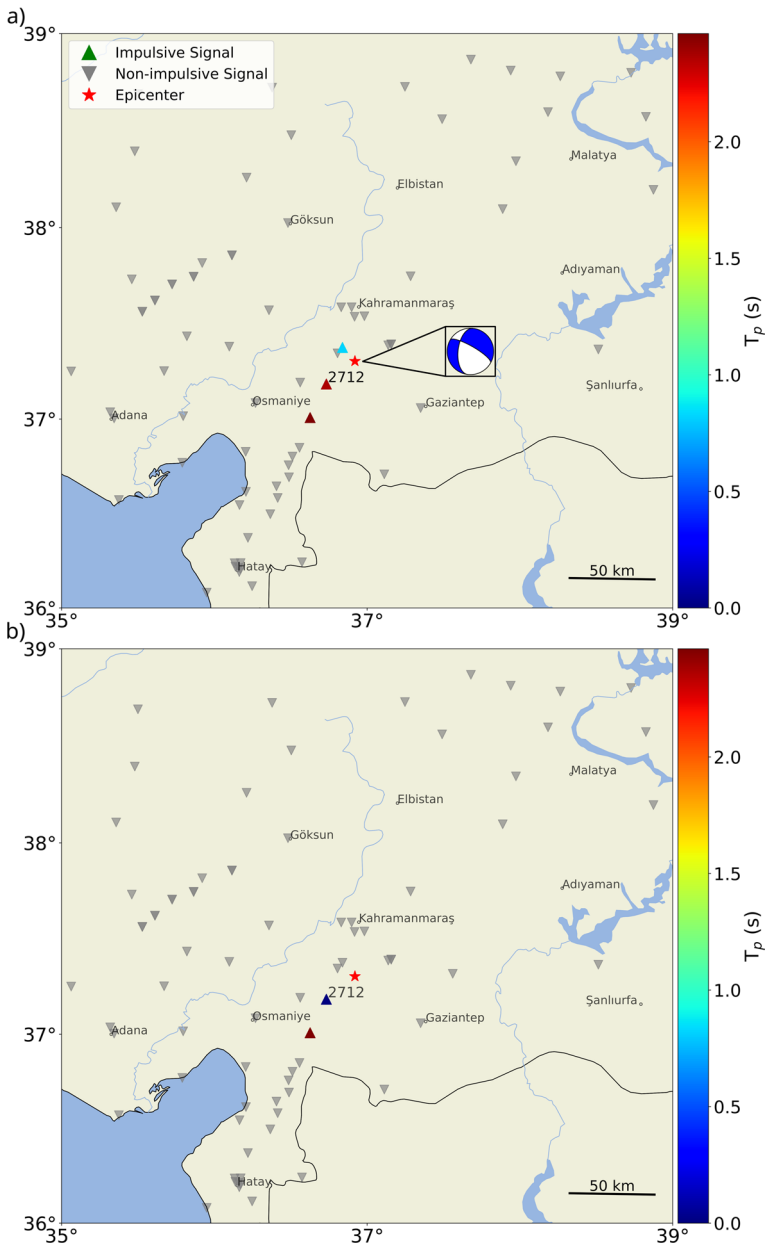


Fig. 9 Impulsive signals detected by **a**Shahi and Baker (2014) **b** Ertuncay and Costa (2019) in Nurdagi earthquake. The red star is the epicenter of the event. Both the epicenter and the focal mechanism are retrieved from the AFAD catalogue

Even though the number of impulsive signals is lower than for the Pazarcık earthquake, there are a significant number of impulsive signals recorded for the Elbistan earthquake (Fig. 11). Station coverage around the fault plane is not as good as the

Table 5 Parameters of impulsive signals in Nurdağı earthquake

Station	Component	STLA	STLO	Vs30 (cm s ⁻¹)	R _{epi} (km)	PGA (cm s ⁻²)	PGV (cm s ⁻¹)	T _p Ertuncay and Costa (2019) [s]	T _p Shahi and Baker (2014) [s]
2712	FP	37.18	36.73	495*	21.29	509.88	38.39	0.0	0.64
	FN					303.33	23.43	2.54	0.0
	Ver					360.32	22.8	0.0	2.37
2718	FN	37.01	36.63	415*	41.95	212.85	23.2	2.14	2.46
	FP	37.38	36.84	390	10.74	272.72	29.84	0.0	1.6
4616	FN					246.1	19.18	0.0	0.83

Vs30s with * are predicted by the method of (Oktaş 2022) due to a lack of information on the AFAD website. FP, FN, and Ver. represent fault-parallel, fault-normal, and vertical components

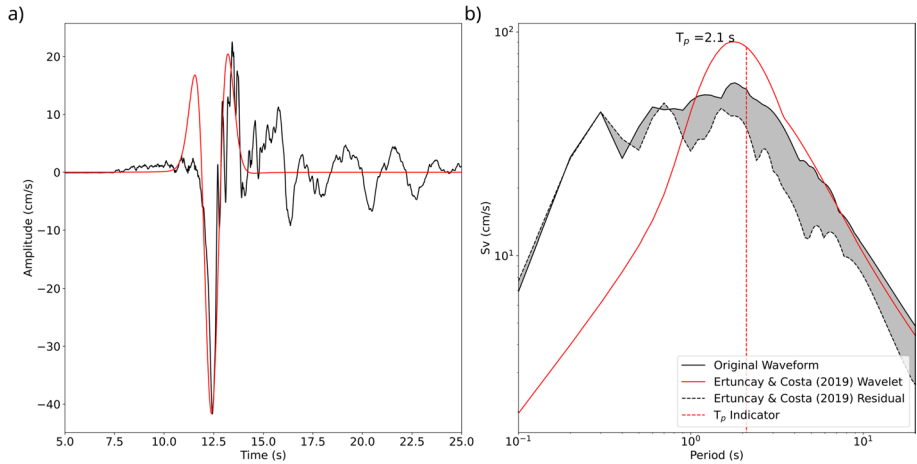


Fig. 10 **a** Velocity time history of Station 2718 in Nurdağı earthquake (black) and the fitted wavelet (red) by the Ertuncay and Costa (2019) method and **b** velocity response spectra of the station, the wavelet, and the residuals between the velocity waveform and the wavelet. Grey area defines the contribution of the impulsive part of the signal on the velocity response spectra

Pazarcık earthquake, with only one station on top of the fault ($R_{jb} = 0$ km). Impulsive motions for the Elbistan earthquake also reached up to $R_{jb} \approx 150$ km (Fig. 12). Keep in mind that the epicentre of the earthquake is not located on the ruptured fault, since epicentre information is retrieved from AFAD, whereas the finite fault model is retrieved from Survey USG (2023b), which creates differences in the distances given in Fig. 12. However, it does not create significant changes, and has no bearing on the results of this study. Due to the proximity of Station 4611 to the ruptured fault, most of the seismic energy is concentrated at the beginning of the signals, whereas in other impulsive stations, there are various trends. In stations such as NAR and Station 0131, seismic energy is concentrated into a single long-period waveform, whereas stations such as Station 2703 and Station 0118 show more complex seismic traces with seismic traces that are energetic over longer time spans.

To detect impulsive motion, stations are rotated from East–West and North–South orthogonal components to fault-normal and fault-parallel components by using the strike angles of each segment, which are 276° , 60° , and 250° . In total Shahi and Baker (2014) and Ertuncay and Costa (2019) found 26 and 5 impulsive signals, respectively. Among the impulsive motions, 9 and 1 of them are in fault-parallel, 11 and 3 of them are in fault-normal, and finally, 6 and 1 of them are in vertical components for Shahi and Baker (2014) and Ertuncay and Costa (2019) methods, respectively (Table 6). The pulse period of impulsive motions in the earthquake can reach up to 11 s in Station 0133 (Fig. 13). In Station 0133, seismic energy is concentrated into a single pulse that excites the spectral energies between 6 and 11 s. The wavelet fitted by the Shahi and Baker (2014) method represents the impulsive behaviour of the station as the spectral energies of the residual waveform have no such distinctive peaks at these periods.

The probability of occurrence is calculated as in Sect. 4.3. In Elbistan, earthquake probability results differ from one another (Fig. 14). There are widespread impulsive signals at longer distances to the South and South–West of the fault rupture, which provides a considerable amount of the total impulsive motions identified for the earthquake. The Shahi and

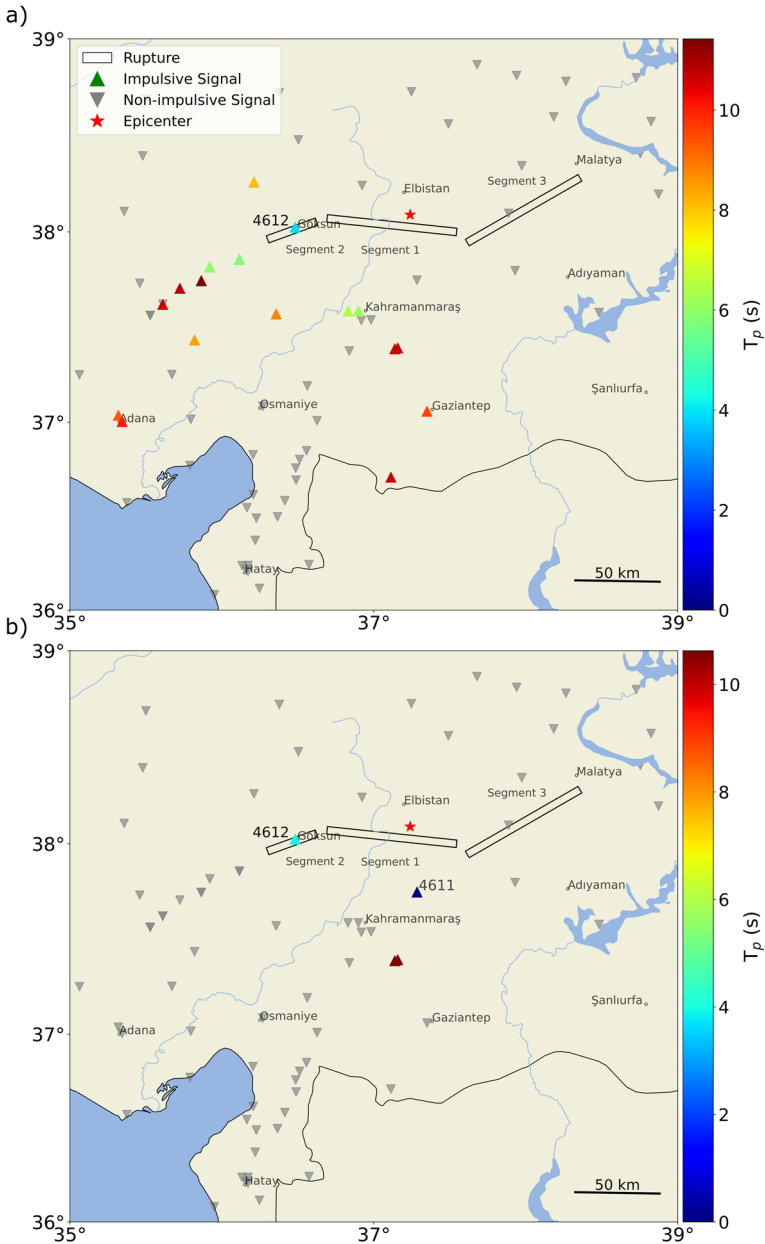


Fig. 11 Impulsive signals detected by **a** the Shahi and Baker (2014) method and **b** the Ertuncay and Costa (2019) method for the Elbistan earthquake. The red star is the epicenter of the event retrieved from AFAD catalog and black boxes are the ruptured segments as defined by USGS (2023b)

Baker (2014) model underestimates impulsive motion at long distances. Due to the fixed PGV threshold of the Ertuncay and Costa (2019) method, the NAR station is the only station in the area with 0 % probability.

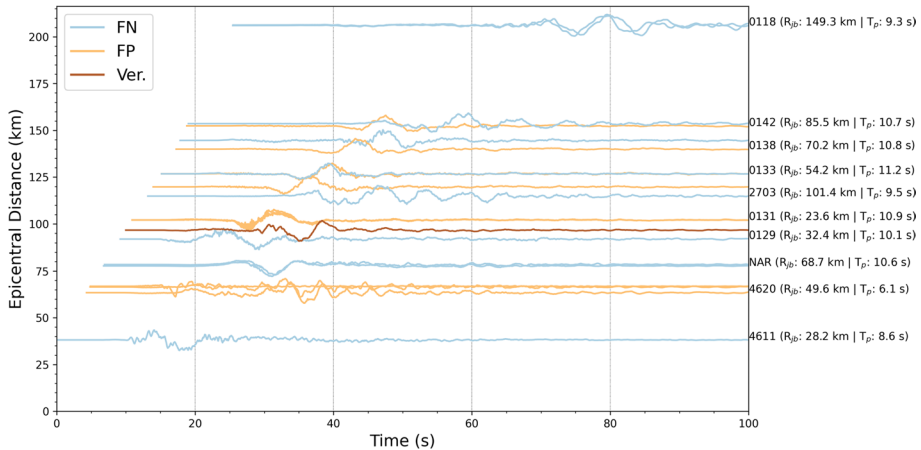


Fig. 12 Velocity time histories of impulsive signals recorded for the Elbistan earthquake. In case of impulsive motions in more than one orientation for a given station, the velocity time history of the channel with the largest T_p is selected

5 Discussion

For the Pazarcık earthquake, a very complex multi-segment fault rupture occurred, and the rupture's features may have influenced the impulsive motion. Melgar et al. (2023) found that in the EAF section of the Pazarcık earthquake, a sub-shear rupture occurred, whereas the results of Okuwaki et al. (2023) indicate a super-shear rupture in Segment 3. The number of impulsive signals in Segment 3 agrees with Okuwaki et al. (2023) due to the large number of impulsive motions found by both Shahi and Baker (2014) and Ertuncay and Costa (2019) methods.

Somerville et al. (1997) and Burks and Baker (2016) link impulsive motion in near-fault stations to S-wave polarization. Horizontally polarized S-waves (SH) are the main reason for the two-sided impulsive motions in the fault-normal component, which is present in more than half of the impulsive motions found by the Shahi and Baker (2014) method for the Pazarcık earthquake, and vertically polarized S-waves (SV) may be linked to the Gaussian-like pulses. There are 25 and 17 fault-parallel impulsive motions at present in the Pazarcık earthquake detected by Ertuncay and Costa (2019) and Shahi and Baker (2014), respectively. However, not all of the velocity time histories are Gaussian-like and have impulsive motions that are more complex than a simple Gaussian-like wavelet.

Stations NAR, KHMN, and 4615 are located next to the NPF fault where the rupture initiated and only a small portion of the seismic moment was released (3 %, Okuwaki et al. 2023). These stations, however, recorded impulsive motions between $T_p \approx 3.5$ s–5.0 s, which can be linked to the super shear rupture velocity around the tip of the NPF (Rosakis et al. 2023). Satoh (2023) also points out the significance of local super shear rupture on NAR and Station 4615.

The distribution of impulsive signals shows the transition between S-wave-driven and surface wave-driven impulsive signals. For the Pazarcık earthquake (Fig. 5), Station 4615 is very close to the epicenter and Segment 1 of the earthquake, and R_{jb} distances are close to 0 km, and most of the seismic energy is concentrated between 10 s and 15 s after the origin time. For Station 4615 and Station 3115, impulsive motions are

Table 6 Parameters of impulsive signals for the Elbistan earthquake

Station	Component	STLA	STLO	Vs30 (cm s ⁻¹)	R _{ip} (km)	PGA (cm s ⁻²)	PGV (cm s ⁻¹)	T _p Ertuncay and Costa (2019) [s]	T _p Shahi and Baker (2014) [s]
0118	FN	37.04	35.32	479*	149.34	26.62	23.22	0.0	9.3
0122	FN	37.43	35.82	473*	78.48	71.73	17.89	0.0	8.44
0123	FN	37.0	35.34	250*	149.79	26.54	22.03	0.0	10.09
0127	FP	37.82	35.92	704*	45.17	61.65	21.62	0.0	11.03
	Ver					35.65	17.19	0.0	6.01
0129	FN	38.26	36.21	515*	32.41	130.26	16.93	0.0	10.08
	Ver					86.37	16.12	0.0	8.09
0131	FP	37.86	36.12	717*	23.6	491.37	28.48	0.0	10.86
	Ver					83.99	19.84	0.0	5.84
0132	FP	37.86	36.11	717*	23.68	67.79	19.19	0.0	11.1
	Ver					56.96	19.77	0.0	5.8
0133	FP	37.75	35.86	548*	54.15	58.79	19.81	0.0	11.19
	FN					66.95	16.62	0.0	4.83
0134	FN	37.74	35.86	548*	54.16	54.56	22.48	0.0	11.42
0138	FP	37.7	35.72	629*	70.25	24.44	16.81	0.0	10.84
0142	FP	37.62	35.61	648*	85.5	26.3	17.19	0.0	10.65
2703	FN	37.06	37.35	758	101.45	64.43	23.02	0.0	9.53
4611	FN	37.75	37.28	731	28.19	135.46	32.23	8.55	0.0
4612	FP	38.02	36.48	246	0.0	597.4	164.13	5.09	6.38
	Ver					443.95	47.76	3.6	3.91
4613	FN	37.57	36.36	998	41.77	62.84	17.94	0.0	6.8
	Ver					77.45	19.14	0.0	8.78
4615	FN	37.39	37.14	484	69.47	75.95	34.28	10.17	10.63

Table 6 (continued)

Station	Component	STLA	STLO	Vs30 (cm s ⁻¹)	R _{fp} (km)	PGA (cm s ⁻²)	PGV (cm s ⁻¹)	T _p Ertuncay and Costa (2019) [s]	T _p Shahi and Baker (2014) [s]
4617	FP	37.59	36.83	574	50.27	53.04	28.15	0.0	6.44
4620	FP	37.59	36.9	484	49.63	73.72	23.33	0.0	6.12
7901	FN	36.71	37.11	463	144.84	51.66	21.92	0.0	10.68
NAR	FN	37.39	37.16	248*	68.72	115.9	31.72	10.17	10.63

Vs30s with * as predicted by the (Oktyay 2022) method due to a lack of information on the AFAD website. FP, FN, and Ver. represent fault-parallel, fault-normal, and vertical components

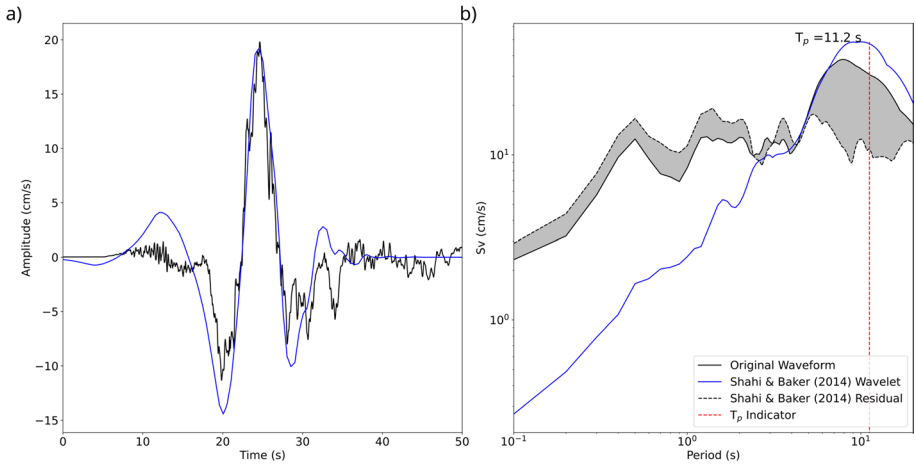


Fig. 13 **a** Velocity time history of Station 0133 in Elbistan earthquake (black) and fitted wavelet (blue) by the Shahi and Baker (2014) method and **b** velocity response spectra of the station, the wavelet, and residuals between the velocity waveform and the wavelet. The grey area defines the contribution of the impulsive part of the signal on the velocity response spectra

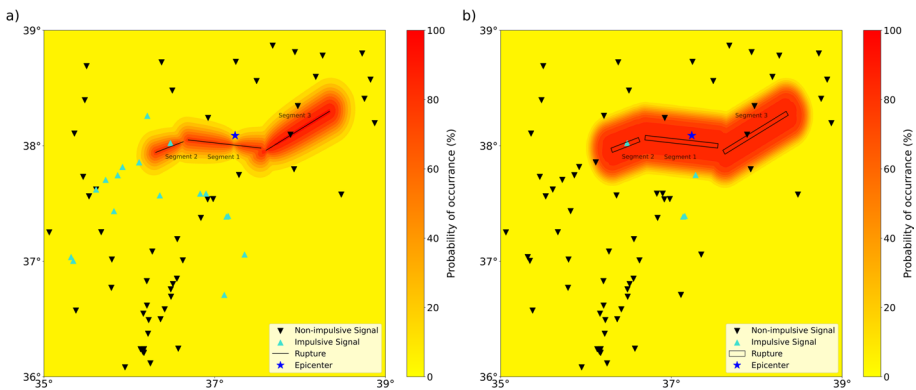


Fig. 14 Probability of observing impulsive motions **a** the Shahi and Baker (2014) method and **b** the Ertuncay and Costa (2021) method for the Elbistan earthquake. The blue star is the event epicentre, and black and turquoise triangles are the non-impulsive and impulsive stations, respectively

caused by the S-waves, but in Station 0120 a more complex seismic trace is observed, and the impulsive motion is located more toward the end of the S-wave. It is possible that surface waves played a part in the impulsive motion. Station 3124 and other nearby impulsive motions in Hatay are located on top of Segment 3. It is important to point out that complex, multi-segment rupture enriched the seismic waveforms differently. In Station 4615, the rupture of Segment 1 is the main contributor to the seismic trace; in Station 3125 the effect of Segment 1 and even Segment 2 are significantly smaller. Hence for this station there are small ground motions between 50 s and 75 s after the origin time, and the effect of Segment 3 is visible after 75 s. Satoh (2023) also finds that in the northern part of Segment 3, various areas in the ruptured zone are responsible

for the strong ground motion. This can be linked to widespread impulsive motion in the upper and central part of Segment 3 and its surroundings. For the Elbistan earthquake (Fig. 12), a similar trend can be identified. Impulsive signals up to 150 km R_{jb} distance are located in the S-wave, with the exception of Station 2703 where the R_{jb} distance is more than two times larger than the others. For stations with R_{jb} distances larger than 100 km, impulsive motions are located toward the later stages of the seismic waves.

The probability calculation method of Shahi and Baker (2014) calculates the probability of observing an impulsive signal around the epicentral area of the Pazarçık earthquake as being over 90 % whereas the Ertuncay and Costa (2021) method gives a maximum value of 85 %. For the Shahi and Baker (2014) method, the width of the high percentage zone is related to the fault length, where the widest area with the largest percentages is Segment 3 of the Pazarçık earthquake. Super-shear rupture on Segment 2 of the earthquake produced a large amount of impulsive motion even though the width of the impulsive motion is narrower than Segment 2 due to the shorter length of the segment. The Ertuncay and Costa (2021) method does not affect the fault length as M_w is the main source of the impulsive motions. Even though the maximum percentage of the model is lower than the Shahi and Baker (2014) method, also having non-impulsive motions around the R_{jb} area lowers the actual percentage of impulsive signals around the fault lines (Fig. 15).

For the Elbistan earthquake the Shahi and Baker (2014) method underestimates the probability of observing impulsive motion due to a large amount of impulsive motions detected to the south and southwest of the ruptured faults. The percentage of impulsive motions increases with distance, unlike the expected descending trend. It must be taken into consideration, however, that seismic stations are not evenly distributed, and this may amplify the apparent impulsive motion percentage. Widespread impulsive motion over long distances is an unexpected finding, which makes it hard to predict long-period signals. Moreover, impulsive motion on the western part of the ruptured fault can be linked to super shear rupture features of the earthquake (Melgar et al. 2023). Since the length of the fault is the driving force of the impulsive motion for the Shahi and Baker (2014) method, Segment 2 has the highest probability of generating impulsive motion. The Ertuncay and Costa (2021) method successfully predicts the impulsive motion at Station 4612, whereas the other three impulsive motions that are identified by the Ertuncay and Costa (2019) method are located in the areas with low probability of occurrence.

For the Pazarçık and Elbistan earthquakes, longer period pulses agree with the Shahi and Baker (2014); Ertuncay (2020) methods and short periods pulses are in agreement with the Somerville (2003), Bray and Rodriguez-Marek (2004) methods (Fig. 16). Standard deviations (STDs) generated by the Shahi and Baker (2014), Ertuncay (2020) methods covered all long-period signals but failed to capture the short-period ones. Predictions of Somerville (2003) for rock sites are almost entirely covered thanks to their large standard deviation, but none of the stations are located in rock sites (Table 1), and the model for soil sites also failed to cover the short period signals. The prediction by the Bray and Rodriguez-Marek (2004) methods are similar to the prediction of the Somerville (2003) methods. The models for soil and rock sites converge around magnitude 7.7, and both models underestimate long-period impulsive motion. The importance of impulsive motion, however, is in the long-period features, and the methods of Shahi and Baker (2014), Ertuncay (2020) performed well over long periods and Somerville (2003) covers the long periods due to its σ . Models developed by Bray and Rodriguez-Marek (2004) perform relatively badly at long periods.

Even though impulsive motions are more dominant in FP and FN components, previous studies show that they are not the only orientation in which the maximum pulse may be

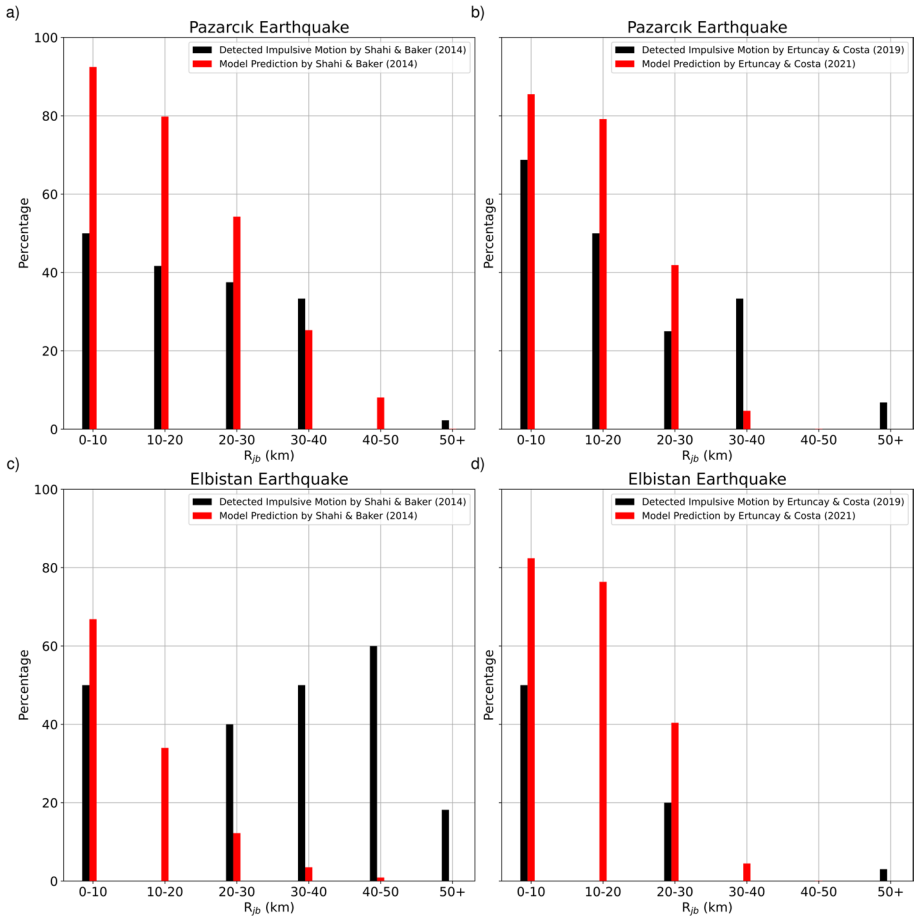


Fig. 15 Spatial distribution of the percentage of impulsive motions detected by **a, c** the (Shahi and Baker 2014) method, and **b, d** the (Ertuncay and Costa 2019) method, along with the average probability of pulse occurrence predicted for the **a, b** Pazarçık and **c, d** Elbistan earthquakes

observed (Shahi and Baker 2011, 2014). Shahi and Baker (2011) try to find pulses by rotating the given signal in all possible directions to maximize finding impulsive motion, which may lead to finding false-positive impulsive motion (Shahi and Baker 2014). Shahi and Baker (2014) overcome this problem by rotating the 2 orthogonal components to find the maximum pulse with its direction as explained in Sect. 3. To find impulsive motions with the largest pulse direction, we provide the horizontal components of the signals (Fig. 17). As expected in both earthquakes, near-fault pulses mostly agree with the fault plane (FN) or its orthogonal (FP) direction. There are several stations, however, that do not follow this general trend. For instance, several stations in Hatay have their maximum pulse direction at $\approx 45^\circ$. In Hatay city, the impulsive motions are positioned in the later stages of the seismic waveform (Fig. 5), and the V_{s30} values at the stations are relatively low. Both complex rupture features and local soil conditions may affect the ground motion and create impulsive motion in this direction. Several stations where Segment 1 and Segment 3 meet also have maximum pulse direction at $\approx 45^\circ$, and again, this peculiar direction can be linked to

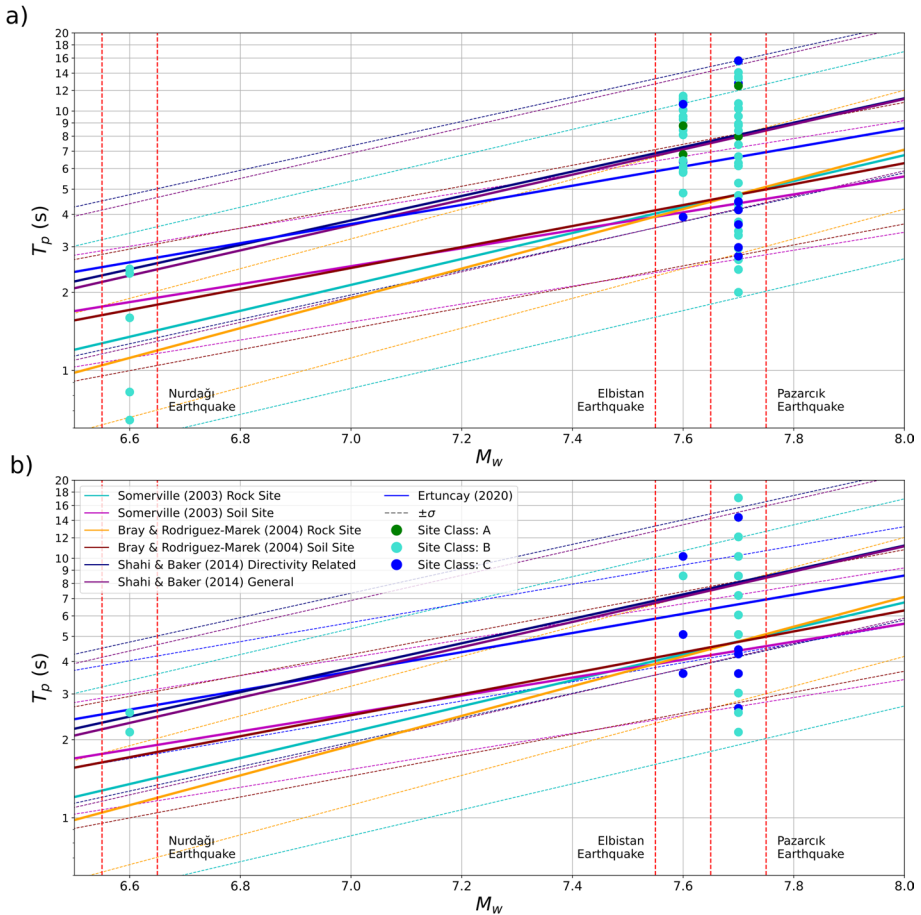


Fig. 16 Periods of impulsive motions determined by **a** the Shahi and Baker (2014) method, and **b** the Ertuncay and Costa (2019) method along with pulse periods determined by the Somerville (2003), Bray and Rodriguez-Marek (2004), Shahi and Baker (2014), Ertuncay (2020) models. Dashed lines define the standard deviations of the models

the rupture features. Since revealing their behaviour is not the topic of this study, we do not carry out further investigation into the forces that played a role in the direction of the impulsive motions, but we nonetheless prefer to report the observations that we retrieve. For the Elbistan earthquake Station 4612 and stations on the South-West of Segment 2 are in agreement with the FN direction of the segment. Other stations, however, are in different directions with respect to the others. Those stations are located away from the near-fault area, and surface waves may be the dominant force on the East–West orientation of the impulsive motion. Moreover, a number of impulsive signals and stations with impulsive features presented for both the Pazarcık and Elbistan earthquakes are different in Fig. 17. It is due to the fact that, to find the direction of the pulse, orthogonal components are given as inputs, whereas in the previous section the components are given individually. Those differences are considered as "false-positives" by Shahi and Baker (2014). Our main idea, however, is to find impulsive motions in the 3 fundamental components, namely FN, FP,

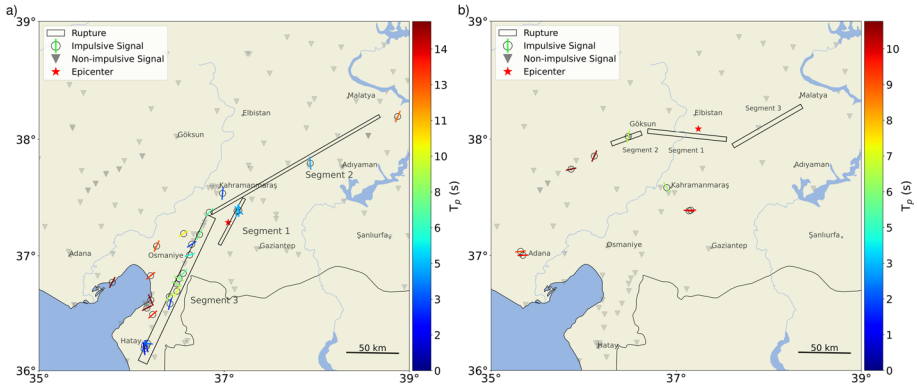


Fig. 17 Direction of the strongest pulses in the **a** Pazarcık and **b** Elbistan earthquakes detected by the Shahi and Baker (2014) method. The red star is the epicentre of the event; black triangles are non-impulsive stations, and black circles with coloured lines are impulsive stations. The color of the lines represents the pulse period

and vertical. Thus we do not consider them as "false positives" but as actual impulsive signals.

Long-period signals may create large seismic loads on structures (Kalkan and Kunath 2006). When the pulse period of the impulsive motion is similar to the fundamental period of a given structure, it can be the main source of the building response and may create a resonance effect (Archila et al. 2017; Takewaki et al. 2011). For this purpose, finding the dominant periods of the ground motion is important. In both the Pazarcık and Elbistan earthquakes, a wide range of pulse periods are found (Fig. 16); some of them have periods even longer than 10 s. Stations such as NAR, 4611, and

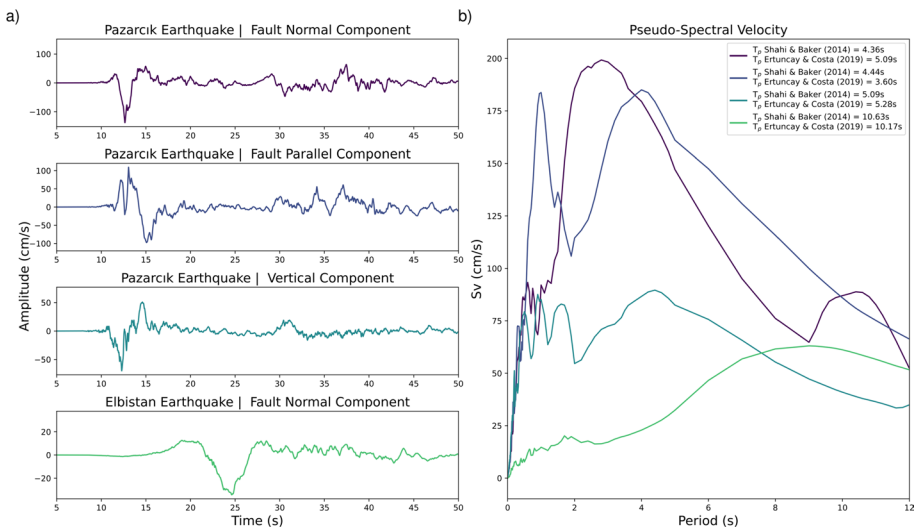


Fig. 18 **a** Seismic records of the Pazarcık, Nurdağı, and Elbistan earthquakes for Station 4615 and **b** their pseudo-spectral velocities (Sv.)

4615 recorded impulsive motion in two of the three earthquakes (Fig. 18). In the town of Narlı, where the station NAR is located, there are most of the buildings have 2–3 stories buildings with relatively low damage. On the other hand, numerous tall buildings collapsed on the 6th of February in the cities of Hatay, Kahramanmaraş, and Adana. Construction flaws, insufficient building design principles, and/or the cumulative effects of several earthquakes may have played a role in their collapse (Vuran et al. 2024), but investigation of the collapsed buildings is not in the scope of this study. In some of the stations with impulsive motions, however, the response spectra of the ground motion exceeds the current building design code of Türkiye (Fig. 19 Akkar et al. 2018).

Impulsive signals are known for their large PGV values (Moustafa and Takewaki 2010). In both the Pazarcık and Elbistan earthquakes, large PGV values are observed (Fig. 20). To compare the PGVs with the ground motion prediction equation (GMPE), we use the Kale et al. (2015) (KALE15) model, since it was created for Türkiye and Iran using earthquakes and seismic records from these regions. As seen in Fig. 20, the Kahramanmaraş earthquakes produced a large number of ground motion records that surpass the prediction of the KALE15 model. For impulsive motions detected by the Shahi and Baker (2014) method there is only one station (in Pazarcık) that is within and close to the border of the +1 STD of the prediction. Both of the earthquakes produced PGVs larger than the predicted values independent from being impulsive, which can be linked to the directivity effect (Bray and Rodriguez-Marek 2004). In the residual analysis of the PGVs, stations located on top of the rupture zone ($R_{jb} = 0$ km) have a very large difference from the median values of the GMPEs, and the difference diminishes around 100 km for the Pazarcık earthquake. In the rupture area ($R_{jb} = 0$ km), it is expected to have an underestimation of the GMPE model due to the complex physics of large magnitude earthquakes and lack of observed waveforms from near-fault stations. On the other hand, the Elbistan earthquake created larger ground motions than expected by the KALE15 model, even at longer distances. Extensive stress accumulated around the region after the Pazarcık earthquake may be linked to the unexpectedly large ground motion as there is a correlation between stress drop and ground motion variability (Oth et al. 2017). All impulsive motions have larger amplitudes compared to predictions from the KALE15 method.

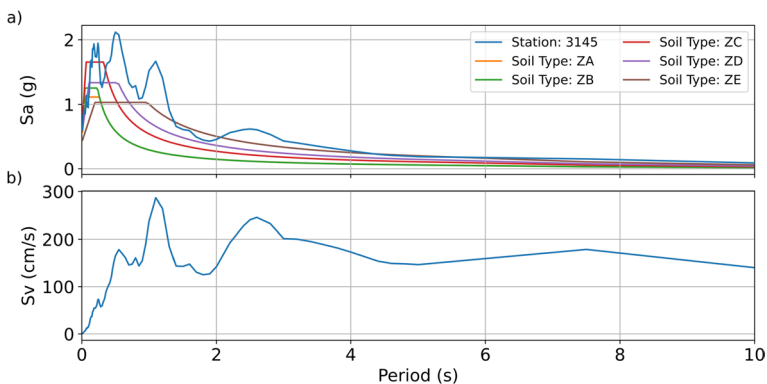


Fig. 19 **a** Spectral acceleration (S_a) of the fault-normal channel for Station 3145 along with the 2018 Turkish design code for 10 % probability of exceedance in 50 years for different soil classes, **b** pseudo-spectral velocity (S_v)

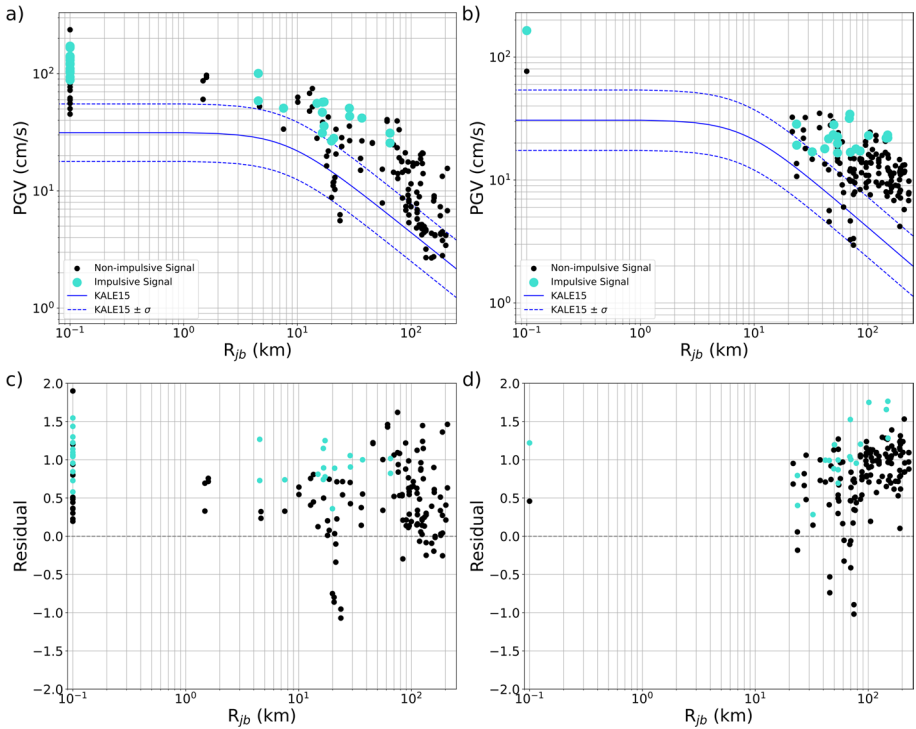


Fig. 20 Observed PGVs of the **a** Pazarcık, **b** Elbistan earthquakes for horizontal components compared to the GMPE model of Kale et al. (2015) and the residuals of the observed and predicted PGVs for the **c** Pazarcık, and **d** Elbistan earthquakes. Turquoise and black circles are PGVs of impulsive and non-impulsive signals determined by the Shahi and Baker (2014) method, respectively. Stations located on top of the fault ($R_{jb} = 0$ km) are moved to 0.1 km for visualization

Unusually, the Pazarcık earthquake produced a large number of vertical component impulsive motions. Historically, horizontal ground motions are generally stronger than vertical ones. In fact, vertical ground motions attenuate faster than horizontal motions in the far-field (Campbell 1997). Recent studies reveal, however, that in near-fault regions, vertical ground motion can also have large amplitude and have significant effects on structures (Bozorgnia and Campbell 2004). The Kahramanmaraş earthquakes are in agreement with recent studies with PGVs up to 100 cm s^{-1} (Fig. 21). The largest PGV in the vertical component is a spike-like waveform in Station 3138, which can be linked to the flapping effect that can be observed when the base of the station is not well connected to the ground and bounced during ground shaking (Goto et al. 2019), meaning that impulsive motions detected at this station are not trustworthy. Other vertical component impulsive signals, however, do not have this anomaly, and they are produced by real ground motion (Fig. 22).

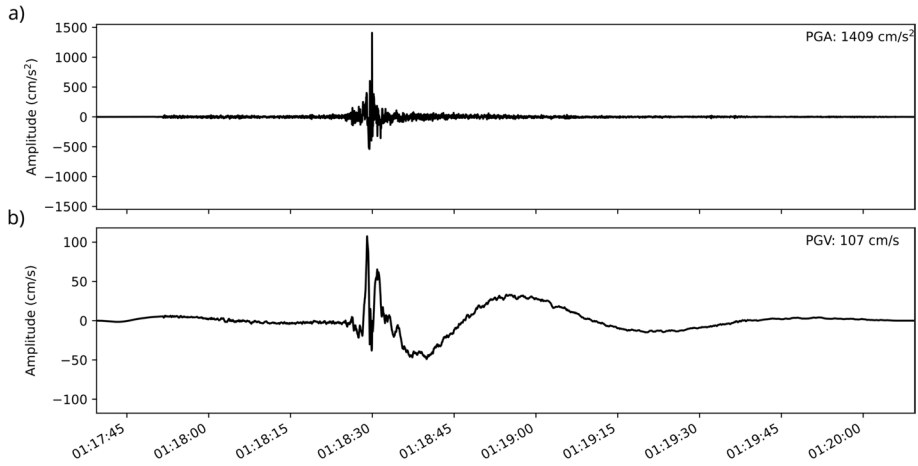


Fig. 21 **a** Acceleration and **b** velocity time histories recorded for the Pazarçık earthquake on the vertical component of Station 3138

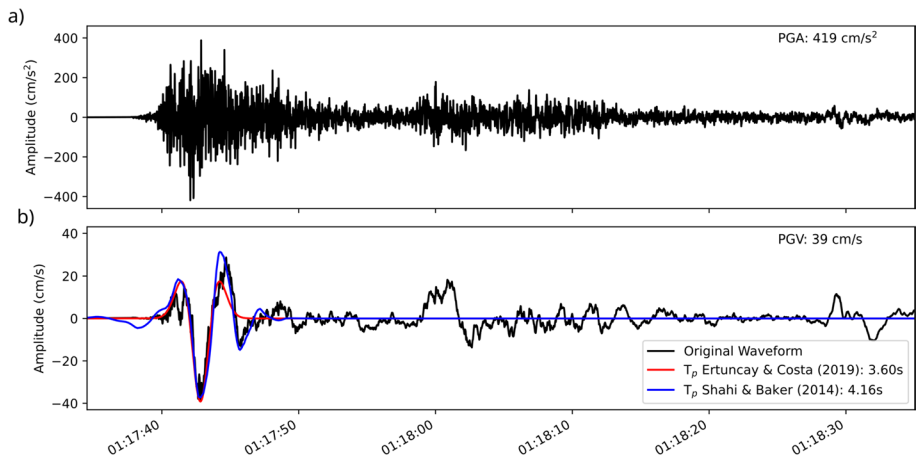


Fig. 22 **a** Acceleration and **b** velocity time history along with the extracted pulses by the Shahi and Baker (2014), Ertuncay and Costa (2019) methods for the Station KHMN record in for the Pazarçık earthquake

6 Conclusion

In this study we find that during the Kahramanmaraş earthquakes 3 earthquakes produced, in total, 72 and 62 impulsive motions according to the methods of Shahi and Baker (2014), Ertuncay and Costa (2019), respectively. The periods of the impulsive signals reach up to 15.5 s for the Pazarçık earthquake, which has the largest magnitude out of the Kahramanmaraş earthquakes. For the Pazarçık and Elbistan earthquakes, previous studies detected super-shear ruptures, which may be the reason for the abundance of impulsive motions. For the Elbistan earthquake, impulsive motions were observed up to 150 km distance from the fault (Fig. 11), which exceeds the expectation of impulsive signal probability

derived from the Shahi and Baker (2014), Ertuncay and Costa (2021) methods. The models do not necessarily perform badly, however, since stations are not evenly distributed around the region, which may amplify the presence of impulsive motion over a certain distance range. The direction of the most energetic impulsive motions is also analyzed with the Shahi and Baker (2014) method. In both earthquakes, the directions are mostly in alignment with the fault-normal and fault-parallel directions. The direction of the predominant pulses in Hatay, on the other hand, is slightly different from the other impulsive stations in which local soil conditions and earthquake rupture may play a role. Long-period impulsive motions exceed the current design codes of Türkiye, which may create unexpected damage even in newly built high-rise buildings. PGV values are also higher than the GMPE model of Kale et al. (2015), which is produced for the region. Surprisingly, numerous impulsive motions are located in the vertical component. Strike-slip faults are known to have relatively low amplitude vertical ground motion, but for the Kahramanmaraş earthquakes, this assumption is falsified. The Kahramanmaraş earthquakes and the dense near-fault seismic network provided crucial information about the near-fault effects of large-magnitude earthquakes. This study shows how previous models of impulsive motion performed for the Kahramanmaraş earthquake, and future studies may initiate by analyzing our results to understand long-period ground motion and its possible effects on structures and infrastructure better.

Acknowledgements We thank two anonymous reviewers for their constructive comments and Jonathan Ford for proofreading the paper. We also thank Rıdvan Örsvuran from Colorado School of Mines for his mass data downloader code (https://rdno.org/git/rdn/tdvms_py), which helped us immensely in retrieving a large quantity of seismic data.

Author Contributions All authors contributed to the study's conception and design. Deniz Ertuncay performed material preparation, data collection and analysis. Deniz Ertuncay wrote the first draft of the manuscript, and all authors commented on previous versions of the manuscript. All authors read and approved the final manuscript.

Funding Open access funding provided by Istituto Nazionale di Oceanografia e di Geofisica Sperimentale within the CRUI-CARE Agreement. This research received financial support from the Italian Civil Protection Department-Presidency of the Council of Ministers (DPC) under the agreement between DPC and the University of Trieste for the accelerometric monitoring of the Friuli Venezia Giulia Region (Number Agreement: RAN2020-2022 CUP J91F20000110001) and RETURN Extended Partnership and received funding from the European Union Next-GenerationEU (National Recovery and Resilience Plan-NRRP, Mission 4, Component 2, Investment 1.3-D.D. 1243 2/8/2022, PE0000005, CUP F83C22001660002).

Data availability Earthquake data can be retrieved from tdvms.afad.gov.tr/continuous_data.

Declarations

Conflict of interest The authors declare that they have no conflict of interest.

Open Access This article is licensed under a Creative Commons Attribution 4.0 International License, which permits use, sharing, adaptation, distribution and reproduction in any medium or format, as long as you give appropriate credit to the original author(s) and the source, provide a link to the Creative Commons licence, and indicate if changes were made. The images or other third party material in this article are included in the article's Creative Commons licence, unless indicated otherwise in a credit line to the material. If material is not included in the article's Creative Commons licence and your intended use is not permitted by statutory regulation or exceeds the permitted use, you will need to obtain permission directly from the copyright holder. To view a copy of this licence, visit <http://creativecommons.org/licenses/by/4.0/>.

References

- Akkar S, Kale Ö, Yakut A, Ceken U (2018) Ground-motion characterization for the probabilistic seismic hazard assessment in turkey. *Bull Earthq Eng* 16:3439–3463. <https://doi.org/10.1007/s10518-017-0101-2>
- Akkar S, Azak T, Çan T, Çeken U, Demircioğlu Tümsa M, Duman T, Erdik M, Ergintav S, Kadirioglu F, Kalafat D (2018) Evolution of seismic hazard maps in Turkey. *Bull Earthq Eng* 16:3197–3228. <https://doi.org/10.1007/s10518-018-0349-1>
- Ali A, De Risi R, Sextos A, Goda K, Chang Z (2020) Seismic vulnerability of offshore wind turbines to pulse and non-pulse records. *Earthq Eng Struct Dyn* 49(1):24–50. <https://doi.org/10.1002/eqe.3222>
- Ancheta TD, Darragh RB, Stewart JP, Seyhan E, Silva WJ, Chiou BS-J, Wooddell KE, Graves RW, Kottke AR, Boore DM et al (2014) Nga-west2 database. *Earthq Spectra* 30(3):989–1005. <https://doi.org/10.1193/070913EQS197M>
- Archila M, Ventura CE, Liam Finn W (2017) New insights on effects of directionality and duration of near-field ground motions on seismic response of tall buildings. *Struct Design Tall Spec Build* 26(11):1363. <https://doi.org/10.1002/tal.1363>
- Aucun B, Fajfar P, Franchin P, Carvalho E, Kreslin M, Pecker A, Tsionis G, Pinto P, Degee H, Plumier A, Fardis M, Athanasopoulou A, Bisch P, Somja H (2012) Eurocode 8: seismic design of buildings - worked examples. Publications Office (2012). <https://doi.org/10.2788/91658>
- Barbot S, Luo H, Wang T, Hamiel Y, Piatibratova O, Javed MT, Braitenberg C, Gurbuz G (2023) Slip distribution of the February 6, 2023 mw 7.8 and mw 7.6, Kahramanmaraş, turkey earthquake sequence in the east Anatolian fault zone. *Seismica*. <https://doi.org/10.26443/seismica.v2i3.502>
- Bhagat S, Wijeyewickrema AC, Subedi N (2021) Influence of near-fault ground motions with fling-step and forward-directivity characteristics on seismic response of base-isolated buildings. *J Earthq Eng* 25(3):455–474. <https://doi.org/10.1080/13632469.2018.1520759>
- Bolt B (2002) Estimation of strong seismic ground motions. In: *International handbook of earthquake and engineering seismology*, pp 983–1001 (2002)
- Bozorgnia Y, Campbell KW (2004) The vertical-to-horizontal response spectral ratio and tentative procedures for developing simplified v/h and vertical design spectra. *J Earthq Eng* 8(02):175–207
- Bray JD, Rodriguez-Marek A (2004) Characterization of forward-directivity ground motions in the near-fault region. *Soil Dyn Earthq Eng* 24(11):815–828. <https://doi.org/10.1016/j.soildyn.2004.05.001>
- Burks LS, Baker JW (2016) A predictive model for fling-step in near-fault ground motions based on recordings and simulations. *Soil Dyn Earthq Eng* 80:119–126. <https://doi.org/10.1016/j.soildyn.2015.10.010>
- Cambaz MD, Özer M, Güneş Y, Ergün T, Ögütçü Z, Altuncu-Poyraz S, Köseoğlu A, Turhan F, Yilmazer M, Kekovali K et al (2021) Evolution of the Kandilli observatory and earthquake research institute (Koeri) seismic network and the data center facilities as a primary node of eida. *Seismol Res Lett* 92(3):1571–1580. <https://doi.org/10.1785/0220200367>
- Campbell KW (1997) Empirical near-source attenuation relationships for horizontal and vertical components of peak ground acceleration, peak ground velocity, and pseudo-absolute acceleration response spectra. *Seismol Res Lett* 68(1):154–179. <https://doi.org/10.1785/gssrl.68.1.154>
- Carocci CF (2012) Small centres damaged by 2009 l'aquila earthquake: on site analyses of historical masonry aggregates. *Bull Earthq Eng* 10:45–71. <https://doi.org/10.1007/s10518-011-9284-0>
- Chen L-K, Kurtulus A, Dong Y-F, Taciroglu E, Jiang L-Z (2022) Velocity pulse effects of near-fault earthquakes on a high-speed railway vehicle-ballastless track-benchmark bridge system. *Veh Syst Dyn* 60(9):2963–2987. <https://doi.org/10.1080/00423114.2021.1933546>
- Crowley H, Dabbeek J, Despotaki V, Rodrigues D, Martins L, Silva V, Romão X, Pereira N, Weatherill G, Danciu L (2021) European seismic risk model (esrm20). EFEHR Tech Rep. <https://doi.org/10.7414/EUC-EFEHR-TR002-ESRM20>
- Danciu L, Nandan S, Reyes CG, Basili R, Weatherill G, Beauval C, Rovida A, Vilanova S, Sesetyan K, Bard P-Y, et al (2021) The 2020 update of the european seismic hazard model-eshm20: Model overview. EFEHR Tech Rep 1
- Disaster and Emergency Management Authority (1973) Turkish National Strong Motion Network. Department of Earthquake, Disaster and Emergency Management Authority. <https://doi.org/10.7914/SN/TK>. <https://www.fdsn.org/networks/detail/TK/>
- Disaster and Emergency Management Authority (1990) Turkish National Seismic Network. Department of Earthquake, Disaster and Emergency Management Authority. <https://doi.org/10.7914/SN/TU>. <https://www.fdsn.org/networks/detail/TU/>
- Earth Science NRI, Resilience D (2019) K-NET, KiK-net. <https://doi.org/10.17598/NIED.0004>

- Emre Ö, Duman TY, Özalp Ş, Şaroğlu F, Olgun Ş, Elmacı H, Çan T (2018) Active fault database of turkey. *Bull Earthq Eng* 16(8):3229–3275. <https://doi.org/10.1007/s10518-016-0041-2>
- Erdik M (2013) Earthquake risk in turkey. *Science* 341(6147):724–725. <https://doi.org/10.1126/science.1238945>
- Ertuncay, D (2020) Temporal and spatial analysis of near fault stations in terms of impulsive behavior. Master's thesis, Università degli Studi di Trieste
- Ertuncay D, Costa G (2019) An alternative pulse classification algorithm based on multiple wavelet analysis. *J Seismol* 23:929–942. <https://doi.org/10.1007/s10950-019-09845-y>
- Ertuncay D, Costa G (2021) Determination of near-fault impulsive signals with multivariate Naïve Bayes method. *Nat Hazards* 108(2):1763–1780. <https://doi.org/10.1007/s11069-021-04755-0>
- Fayjaloun R, Causse M, Voisin C, Cornou C, Cotton F (2017) Spatial variability of the directivity pulse periods observed during an earthquake. *Bull Seismol Soc Am* 107(1):308–318. <https://doi.org/10.1785/0120160199>
- GNS Science (2020) GeoNet Aotearoa New Zealand Strong Motion Data Products. GNS Science, GeoNet. <https://doi.org/10.21420/X0MD-MV58>. <https://data.gns.cri.nz/metadata/srv/eng/catalog.search#/metadata/25c52e65-dbf9-4687-8343-3ca0b60961c1>
- Gorai S, Maity D (2021) Numerical investigation on seismic behaviour of aged concrete gravity dams to near source and far source ground motions. *Nat Hazards* 105:943–966. <https://doi.org/10.1007/s11069-020-04344-7>
- Goto H, Kaneko Y, Young J, Avery H, Damiano L (2019) Extreme accelerations during earthquakes caused by elastic flapping effect. *Sci Rep* 9(1):1117. <https://doi.org/10.1038/s41598-018-37716-y>
- Gunasekera R, Ishizawa Escudero OA, Daniell JE, Pomonis A, Macabuag JLDC, Brand J, Schaefer A, Romero Hernandez RA, Esper SG (2023) Sarah; Otálora, Khazai, K.D. Bijan; Cox: Global Rapid Post-Disaster Damage Estimation (GRADE) Report : February 6, Kahramanmaraş Earthquakes - Türkiye Report (English). <http://documents.worldbank.org/curated/en/099022723021250141/P1788430aeb62f08009b2302bd4074030fb>
- Hatayama K (2008) Lessons from the 2003 Tokachi-oki, Japan, earthquake for prediction of long-period strong ground motions and sloshing damage to oil storage tanks. *J Seismol* 12:255–263. <https://doi.org/10.1007/s10950-007-9066-y>
- Kaklamanos J, Baise LG, Boore DM (2011) Estimating unknown input parameters when implementing the NGA ground-motion prediction equations in engineering practice. *Earthq Spectra* 27(4):1219–1235. <https://doi.org/10.1193/1.3650372>
- Kale Ö, Akkar S, Ansari A, Hamzehloo H (2015) A ground-motion predictive model for Iran and turkey for horizontal PGA, PGV, and 5% damped response spectrum: investigation of possible regional effects. *Bull Seismol Soc Am* 105(2A):963–980. <https://doi.org/10.1785/0120140134>
- Kalkan E, Kunnath SK (2006) Effects of fling step and forward directivity on seismic response of buildings. *Earthq Spectra* 22(2):367–390. <https://doi.org/10.1193/1.2192560>
- Kandilli Observatory And Earthquake Research Institute, Boğaziçi University: Kandilli Observatory And Earthquake Research Institute (KOERI). International Federation of Digital Seismograph Networks (1971). <https://doi.org/10.7914/SN/KO>. <https://www.fdsn.org/networks/detail/KO/>
- Kennett B, Engdahl E (1991) Traveltimes for global earthquake location and phase identification. *Geophys J Int* 105(2):429–465. <https://doi.org/10.1111/j.1365-246X.1991.tb06724.x>
- Kobayashi H, Koketsu K, Miyake H (2019) Rupture process of the 2018 Hokkaido eastern IBURI earthquake derived from motion and geodetic data. *Earth Planets Space* 71:1–9. <https://doi.org/10.1186/s40623-019-1041-7>
- Li S, Zhang F, Wang J-Q, Alam MS, Zhang J (2017) Effects of near-fault motions and artificial pulse-type ground motions on super-span cable-stayed bridge systems. *J Bridg Eng* 22(3):04016128. [https://doi.org/10.1061/\(ASCE\)BE.1943-5592.0001008](https://doi.org/10.1061/(ASCE)BE.1943-5592.0001008)
- Melgar D, Taymaz T, Ganas A, Crowell B, Öcalan T, Kahraman M, Tsironi V, Yolsal-Çevikbilen S, Valkaniotis S, Irmak TS, Eken T, Erman C, Özkan B, Dogan AH, Altuntaş C (2023) Sub- and super-shear ruptures during the 2023 mw 7.8 and mw 7.6 earthquake doublet in se türkiye. *Seismica* 1:1. <https://doi.org/10.26443/seismica.v2i3.387>
- Moustafa A, Takewaki I (2010) Deterministic and probabilistic representation of near-field pulse-like ground motion. *Soil Dyn Earthq Eng* 30(5):412–422. <https://doi.org/10.1016/j.soildyn.2009.12.013>
- Oktay HB (2022) A new Vs30 prediction strategy taking geology, terrain, and saturation into account: application to Türkiye. Master's thesis, Middle East Technical University
- Okuwaki R, Yagi Y, Taymaz T, Hicks SP (2023) Multi-scale rupture growth with alternating directions in a complex fault network during the 2023 south-eastern türkiye and syria earthquake doublet. *Geophys. Res. Lett.* 50(12):2023–103480. [10.1029/2023GL103480](https://doi.org/10.1029/2023GL103480)

- Oliveira C, Çaktı E, Stengel D, Branco M (2012) Minaret behavior under earthquake loading: the case of historical Istanbul. *Earthq Eng Struct Dyn* 41(1):19–39. <https://doi.org/10.1002/eqe.1115>
- Oth A, Miyake H, Bindi D (2017) On the relation of earthquake stress drop and ground motion variability. *J Geophys Res Solid Earth* 122(7):5474–5492. <https://doi.org/10.1002/2017JB014026>
- Pacor F, Paolucci R, Luzi L, Sabetta F, Spinelli A, Gorini A, Nicoletti M, Marcucci S, Filippi L, Dolce M (2011) Overview of the Italian strong motion database Itaca 1.0. *Bull Earthq Eng* 9:1723–1739. <https://doi.org/10.1007/s10518-011-9327-6>
- Rosakis A, Abdelmeguid M, Elbanna A (2023) Evidence of early supershear transition in the mw 7.8 kahramanmaraş earthquake from near-field records. arXiv preprint [arXiv:2302.07214](https://arxiv.org/abs/2302.07214). <https://doi.org/10.48550/arXiv.2302.07214>
- Satoh T (2023) Broadband source model of the 2023 Mw 7.8 Türkiye earthquake from strong-motion records by Isochrone Backprojection and empirical green's function method. *Seismol Res Lett*. <https://doi.org/10.1785/0220230268>
- Scala A, Festa G, Del Gaudio S (2018) Relation between near-fault ground motion impulsive signals and source parameters. *J Geophys Res Solid Earth* 123(9):7707–7721. <https://doi.org/10.1029/2018JB015635>
- Shabani A, Zucconi M, Kazemian D, Kioumarsı M (2023) Seismic fragility analysis of low-rise unreinforced masonry buildings subjected to near-and far-field ground motions. *Results Eng*. <https://doi.org/10.1016/j.rineng.2023.101221>
- Shahi SK, Baker JW (2011) An empirically calibrated framework for including the effects of near-fault directivity in probabilistic seismic hazard analysis. *Bull Seismol Soc Am* 101(2):742–755. <https://doi.org/10.1785/0120100090>
- Shahi SK, Baker JW (2014) An efficient algorithm to identify strong-velocity pulses in multicomponent ground motions. *Bull Seismol Soc Am* 104(5):2456–2466. <https://doi.org/10.1785/0120130191>
- Somerville PG (2003) Magnitude scaling of the near fault rupture directivity pulse. *Phys Earth Planet Inter* 137(1–4):201–212. [https://doi.org/10.1016/S0031-9201\(03\)00015-3](https://doi.org/10.1016/S0031-9201(03)00015-3)
- Somerville PG, Smith NF, Graves RW, Abrahamson NA (1995) Accounting for near-fault rupture directivity effects in the development of design ground motions. *ASME-PUBLICATIONS-PVP* 319:67–82
- Somerville PG, Smith NF, Graves RW, Abrahamson NA (1997) Modification of empirical strong ground motion attenuation relations to include the amplitude and duration effects of rupture directivity. *Seismol Res Lett* 68(1):199–222. <https://doi.org/10.1785/gssrl.68.1.199>
- Survey USG (2023a) M 7.8 - Pazarcik Earthquake, Kahramanmaraş Earthquake Sequence. <https://earthquake.usgs.gov/earthquakes/eventpage/us6000jllz/finite-fault> Accessed 21 Jun 2023
- Survey USG (2023b) M 7.5 - Elbistan Earthquake, Kahramanmaraş Earthquake Sequence. <https://earthquake.usgs.gov/earthquakes/eventpage/us6000jlqa/finite-fault> Accessed 21 Jun 2023
- Takewaki I, Murakami S, Fujita K, Yoshitomi S, Tsuji M (2011) The 2011 off the pacific coast of tohoku earthquake and response of high-rise buildings under long-period ground motions. *Soil Dyn Earthq Eng* 31(11):1511–1528. <https://doi.org/10.1016/j.soildyn.2011.06.001>
- Vuran E, Serhatoglu C, Timuragaoglu MO, Smyrou E, Bal IE, Livaoglu R (2024) Damage observations of rc buildings from 2023 kahramanmaraş earthquake sequence and discussion on the seismic code regulations. *Bull Earthq Eng*. <https://doi.org/10.1007/s10518-023-01843-3>
- Wells DL, Coppersmith KJ (1994) New empirical relationships among magnitude, rupture length, rupture width, rupture area, and surface displacement. *Bull Seismol Soc Am* 84(4):974–1002. <https://doi.org/10.1785/BSSA0840040974>
- Zhang S, Huang L, Wang G, Ma Y (2021) Seismic performance of frame-bent structures subjected to near-fault ground motions. *J Eng* 2021(8):429–436. <https://doi.org/10.1049/tje.2.12023>

Publisher's Note Springer Nature remains neutral with regard to jurisdictional claims in published maps and institutional affiliations.